bioRxiv preprint doi: https://doi.org/10.1101/2020.07.30.229468; this version posted July 30, 2020. The copyright holder for this preprint (which was not certified by peer review) is the author/funder, who has granted bioRxiv a license to display the preprint in perpetuity. It is made available under aCC-BY-NC 4.0 International license.

Title:

Quantitative sub-cellular acyl-CoA analysis reveals distinct nuclear regulation

Authors:

Sophie Trefely[1,2,3], Katharina Huber[2,3,6], Joyce Liu[2,3,4], Jay Singh[1], Mary Doan[1], Claudia D. Lovell[2,3,5], Michael Noji[2,3,5], Eliana von Krusenstiern[1], Helen Jiang[1], Anna Bostwick[1], Luke Izzo[2,3,5], Steven Zhao[2,3,5], Kenneth C. Bedi Jr[7], J. Eduardo Rame[7], Juliane G. Bogner-Strauss[6], Clementina Mesaros[8], Kathryn E. Wellen[2,3]* & Nathaniel W. Snyder[1]*

*Co-corresponding authors

Affiliations:

[1] Center for Metabolic Disease Research, Lewis Katz School of Medicine, Temple University, Philadelphia, PA 19140 USA

[2] Department of Cancer Biology, University of Pennsylvania, Philadelphia, PA 19104 USA

[3] Abramson Family Cancer Research Institute, University of Pennsylvania, Philadelphia, PA 19104 USA

[4]Biochemistry and Molecular Biophysics Graduate Group, Perelman School of Medicine, University of Pennsylvania, Philadelphia, PA 19104 USA

[5]Cell and Molecular Biology Graduate Group, Perelman School of Medicine, University of Pennsylvania, Philadelphia, PA 19104 USA

[6] Institute of Biochemistry, Graz University of Technology, Graz 8010 Austria

[7]Penn Medicine Heart Failure Mechanical Assist and Cardiac Transplant Center, Hospital of the University of Pennsylvania, Philadelphia, PA 19104 USA

[8]Department of Pharmacology, University of Pennsylvania, Philadelphia, PA 19104 USA

Corresponding authors address:

Nathaniel W. Snyder
Email: NateWSnyder@temple.edu
Phone: (215) 571-3492
Post: 455 Medical Education Research Building
3500 N Broad St, Philadelphia, PA 19140
USA

Kathryn E. Wellen
Email: wellenk@upenn.edu
Phone: (215) 746-8599
Post: 421 Curie Blvd, 653 BRB II/III
Philadelphia, PA 19104-6160
USA

bioRxiv preprint doi: https://doi.org/10.1101/2020.07.30.229468; this version posted July 30, 2020. The copyright holder for this preprint (which was not certified by peer review) is the author/funder, who has granted bioRxiv a license to display the preprint in perpetuity. It is made available under aCC-BY-NC 4.0 International license.

Summary:
Metabolism is highly compartmentalized within cells, and the sub-cellular distribution of metabolites determines their use. Quantitative sub-cellular metabolomic measurements can yield crucial insights into the roles of metabolites in cellular processes. Yet, these analyses are subject to multiple confounding factors in sample preparation. We developed Stable Isotope Labeling of Essential nutrients in cell Culture - Sub-cellular Fractionation (SILEC-SF), which uses rigorous internal standard controls that are present throughout fractionation and processing to quantify metabolites in sub-cellular compartments by liquid chromatography-mass spectrometry (LC-MS). Focusing on the analysis of acyl-Coenzyme A thioester metabolites (acyl-CoAs), SILEC-SF was tested in a range of sample types from cell lines to mouse and human tissues. Its utility was further validated by analysis of mitochondrial versus cytosolic acyl-CoAs in the well-defined compartmentalized metabolic response to hypoxia. We then applied the method to investigate metabolic responses in the cytosol and nucleus. Within the cytosol, we found that the mevalonate pathway intermediate 3-Hydroxy-3-methylglutaryl-CoA (HMG-CoA) is exquisitely sensitive to acetyl-CoA supply. The nucleus has been an exceptionally challenging compartment in which to quantify metabolites, due in part to its permeability. We applied the SILEC-SF method to nuclei, identifying that the nuclear acyl-CoA profile is distinct from the cytosolic compartment, with notable nuclear enrichment of propionyl-CoA. Altogether, we present the SILEC-SF method as a flexible approach for quantitative sub-cellular metabolic analyses.

Key words:
Sub-cellular, metabolomics, acyl-CoA, internal standard, nucleus, mitochondria

Introduction:

Quantitative measurements of metabolites can yield crucial insights into their roles in cellular processes. However, metabolism is highly compartmentalized within cells, and the concentration and sub-cellular distribution of metabolites determines their use. Whole cell analyses often provide insufficient information on compartment-specific metabolism, particularly when the compartment of interest accounts for a small fraction of whole cell levels of a given metabolite. Indeed, recent advances in fractionation methodologies for compartment-specific metabolite quantitation have yielded important biological insights (Chen et al., 2017; Wyant et al., 2017). Yet, distinct challenges in measuring metabolites in subcellular compartments remain. In particular, sub-cellular fractionation is inherently disruptive and metabolic analysis after fractionation is subject to multiple confounding factors (Dietz, 2017; Lu et al., 2017; Trefely et al., 2019).

Acyl-Coenzyme A thioesters (acyl-CoAs) are a family of reactive metabolites that are involved in multiple metabolic pathways (Trefely et al., 2020). Acetyl-CoA, for example, is the product of multiple catabolic processes in the mitochondria, whilst in the cytosol it is the primary substrate for anabolic processes including de-novo lipid and cholesterol synthesis. Acetyl-CoA is the acyl-donor for acetylation in all compartments. In the nucleus, acetyl-CoA is a substrate for epigenetic regulation via histone acetylation, and histone acetylation levels have

bioRxiv preprint doi: https://doi.org/10.1101/2020.07.30.229468; this version posted July 30, 2020. The copyright holder for this preprint (which was not certified by peer review) is the author/funder, who has granted bioRxiv a license to display the preprint in perpetuity. It is made available under aCC-BY-NC 4.0 International license.

been correlated with cellular acetyl-CoA levels (Cluntun et al., 2015; Lee et al., 2014).The nucleus and cytosol are generally considered a continuous metabolic compartment since the nuclear pores are permeable to small molecule metabolites such as acetyl-CoA. Nevertheless, several recent studies have provided evidence of distinct regulation of acetyl-CoA production within the nucleus (Li et al., 2017; Mews et al., 2017; Sivanand et al., 2017, 2018; Sun et al., 2019; Sutendra et al., 2014). Histone acylation resulting from other acyl-CoA species, including succinyl-CoA, malonyl-CoA, propionyl-CoA, and butyryl-CoA are also correlated with the cellular abundance of their respective acyl-CoA pools (Simithy et al., 2017), but the subcellular distribution and regulation of these pools has not been determined. Rigorous methodologies for determination of nuclear metabolite levels have not been reported, though such methods would represent an important advance in studying mechanistic links between metabolism and chromatin modification.

We developed Stable Isotope Labeling of Essential nutrients in cell Culture - Sub-cellular Fractionation (SILEC-SF) to address the question of sub-cellular acyl-CoA distribution. This approach builds on the SILEC approach using $^{15}N_1{}^{13}C_3$–vitamin B5 to generate cell lines highly enriched for $^{15}N_1{}^{13}C_3$–labeled acyl-CoAs (Basu et al., 2011; Snyder et al., 2014). SILEC-SF applies SILEC-labeled cells as rigorous internal standard controls introduced prior to fractionation to quantify metabolites in sub-cellular fractions. The use of isotope labeled internal standards spiked into samples as early as possible in processing can correct for a range of factors in analysis by liquid chromatography-mass spectrometry (LC-MS) including processing variability, analyte loss, extraction inefficiency, and ion suppression (Ciccimaro and Blair, 2010; Mann, 2006; Ong, 2012). Thus, SILEC-SF accounts for multiple confounding factors affecting sub-cellular fractionation, sample preparation and analysis. We applied SILEC-SF to the analysis of mitochondrial, cytosolic and nuclear metabolites and reveal distinct metabolic regulation of these compartments.

bioRxiv preprint doi: https://doi.org/10.1101/2020.07.30.229468; this version posted July 30, 2020. The copyright holder for this preprint (which was not certified by peer review) is the author/funder, who has granted bioRxiv a license to display the preprint in perpetuity. It is made available under aCC-BY-NC 4.0 International license.

Results:

SILEC-SF uses whole cell internal standards to control for sample processing

Stable Isotope Labeling of Essential nutrients in Cell culture (SILEC) with isotope labeled ($^{15}N_1{}^{13}C_3$-)vitamin B5 (also known as pantothenate) results in isotope label incorporation into the CoA backbone, which can be detected in acyl-CoA thioesters by LC-MS (**figure 1A**)(Basu et al., 2011; Snyder et al., 2014). Taking advantage of the fact that this allows generation of $^{15}N_1{}^{13}C_3$ labeled internal standards at >99% efficiency within living cells, we designed SILEC-subcellular fractionation (SILEC-SF) to achieve acyl-CoA quantitation in subcellular compartments (**figure 1B**). For this, SILEC cells are harvested in fractionation buffer and then added in equal quantity to each experimental sample, which can be cells or tissues. After SILEC cell addition, cells are separated into subcellular compartments by fractionation. This strategy ensures the internal standard is present as whole cells before any processing for fractionation occurs, as well as in every relevant compartment after fractionation. In this way, the internal standards can account for sample loss that occurs from cell harvest to metabolite extraction. Each fraction is then extracted and analyzed separately by LC-MS and the ratio of the light (acyl-CoA molecules from experimental cells) to heavy (SILEC internal standard molecules) signal intensity is used to determine the quantities within each subcellular compartment across different experimental samples. Co-elution and simultaneous analysis of the analyte with the $^{15}N_1{}^{13}C_3$ labeled internal standard improves quantitative performance(Frey et al., 2016). Thus, SILEC-SF applies internal standards as living whole cells to rigorous metabolite quantification in subcellular fractionation experiments. This approach is complementary to and can be used along with any desired fractionation approach.

Absolute quantitation is achieved using standard curves specific to each fraction

Absolute quantitation within each fraction was achieved using separate standard curves generated for each metabolite within each sub-cellular fraction. Thus, accurate quantitative comparisons can be made across samples within the same fraction. Standard curves were generated by fractionation of additional aliquots of SILEC internal standard cells in parallel with experimental samples, followed by addition of known quantities of unlabeled standards (**supp 1A**). Standard curves plot the light:heavy signal intensity ratio against quantity of unlabeled standard. Curves were strikingly different between sub-cellular fractions (**supp. 1B**). These distinct standard curves likely reflect several factors that vary across different fractions including the relative enrichment of specific acyl-CoA species (i.e. different quantities of SILEC internal standard), extraction efficiency, and matrix effects (Ciccimaro and Blair, 2010). Since the matrix is defined as all the components of the sample except the analyte (Guilbault and Hjelm, 1989), and those components would differ across fractions, we reasoned that the effects of the matrix might be different across fractions. To examine the specific impact of matrix on detection by LC-MS we measured the impact of different sub-cellular matrices on raw signal intensity. SILEC sub-cellular matrices were generated by fractionation of fully labeled SILEC internal standard cells, similar to standard curve generation. Unlabeled acyl-CoA standards, however, were added to the SILEC matrix extracts immediately before LC-MS analysis, as opposed to before extraction, and raw signal intensity for unlabeled acyl-CoA standards was acquired. The variation in unlabeled standard signal intensity across different fractions is

bioRxiv preprint doi: https://doi.org/10.1101/2020.07.30.229468; this version posted July 30, 2020. The copyright holder for this preprint (which was not certified by peer review) is the author/funder, who has granted bioRxiv a license to display the preprint in perpetuity. It is made available under aCC-BY-NC 4.0 International license.

specific to each metabolite (**supp. 1C**). This demonstrates that matrix-specific effects contribute to standard curve variation and highlight the importance of using matrix matched standard curves.

Distinct acyl-CoA profiles define mitochondria and cytosol in diverse cell and tissue types

SILEC-SF was applied to determine the acyl-CoA distribution in mitochondria and cytosol in diverse cells and tissues (**figure 1C-F**). Since the SILEC-SF approach is compatible with any fractionation procedure, it can be applied even to human tissues for clinical studies. Thus, for maximal adaptability across sample types, we employed classical differential centrifugation protocol for isolation of mitochondria and cytosol simultaneously (Clayton and Shadel, 2014; Frezza et al., 2007), with adaptations for speed and purity (**supp. 1D**). Protein distribution in each of the fractions was assessed by Western blot to confirm enrichment of specific resident marker proteins for each compartment (**supp. 1F-I**). SILEC-SF reveals distinctive acyl-CoA profiles defining cytosol and mitochondria in diverse cell and tissue types, including brown adipocytes, fibroblasts, mouse liver and human heart tissue. Succinyl-CoA, acetyl-CoA, and CoASH are the most abundant short chain acyl-CoA species on a whole cell level, consistent with data from direct extraction of matching whole cells and tissues in this study and previous studies (**supp. 1E**)(Bedi et al., 2016; Sadhukhan et al., 2016; Simithy et al., 2017). Notably, CoASH is enriched in the cytosol and succinyl-CoA is generally the dominant acyl-CoA species in the mitochondria, while acetyl-CoA was at similar or greater abundance than succinyl-CoA in the cytosol across these different cell/tissue types. The cellular debris represents material that is not partitioned into either the cytosolic or mitochondrial fractions and is enriched in high-density cellular material including nuclei (**Supp. 1F-I**). It is important to consider all fractions generated in processing since cell homogenization and recovery of target organelles is often incomplete. Thus, the SILEC-SF method discerns distinct acyl-CoA profiles in mitochondria versus cytosol.

SILEC-SF detects distinct mitochondrial adaptation to hypoxia

We next sought to validate the SILEC-SF method using a biologically relevant perturbation with a predictable outcome. Reductive carboxylation of α-ketoglutarate (αKG) occurs in the mitochondria under hypoxia, whereby carbons from glutamine are directed to citrate production and away from succinyl-CoA production (Metallo et al., 2011) (**figure 2A**). Thus, reduced mitochondrial succinyl-CoA levels were anticipated under hypoxia. SILEC-SF was applied to the analysis of succinyl-CoA in the mitochondria and cytosol in cells incubated under 20% (normoxia) and 1% (hypoxia) oxygen. Succinyl-CoA was indeed reduced specifically in the mitochondrial compartment, whilst cytosolic levels remained unchanged, indicating an independently regulated metabolic pool (**figure 2B**).

The impact of hypoxia on the panel of short chain acyl-CoA species quantified was assessed by comparing fold change (hypoxia/normoxia) (**figure 2C**). Hypoxia preferentially impacts mitochondrial metabolites, consistent with reduced mitochondrial oxidative metabolism. Short chain acyl-CoA species were generally suppressed under hypoxia on a whole cell level, with mitochondrial metabolite pools more drastically impacted than cytosolic across multiple short chain acyl-CoA species (**figure 2C,D,** a direct comparison of normoxic and hypoxic acyl-CoA quantitation within each fraction is displayed in **supp. 2A-D**). Comparison of

bioRxiv preprint doi: https://doi.org/10.1101/2020.07.30.229468; this version posted July 30, 2020. The copyright holder for this preprint (which was not certified by peer review) is the author/funder, who has granted bioRxiv a license to display the preprint in perpetuity. It is made available under aCC-BY-NC 4.0 International license.

mitochondrial, cytosolic and whole cell acyl-CoA abundance illustrates the selective impact of hypoxia on mitochondrial metabolism (**figure 2D**).

Cytosolic HMG-CoA is exquisitely sensitive to acetate supply

We next applied the SILEC-SF method to investigate nutrient dependence of acetyl-CoA and downstream metabolites. Within the cytosol, acetyl-CoA is used for generation of malonyl-CoA for fatty acid synthesis and HMG-CoA in the mevalonate pathway for synthesis of sterols and isoprenoids (**figure 3A**). To examine nutritional regulation of subcellular acyl-CoA pools, we leveraged two models of ACLY deficiency, which rely on acetate to supply cytosolic acetyl-CoA via Acyl-CoA Synthetase Short Chain Family Member 2 (ACSS2): *Acly*$^{-/-}$ MEFs (Zhao et al., 2016) and *Acly*$^{-/-}$ murine liver cancer cells (**supp. 3A**). We first investigated the relationship between acetate dose and acyl-CoA abundance in whole cells using direct rapid extraction of metabolites. Cells were incubated in 0, 0.1, or 1 mM acetate for 4 hours (**supp. 3B-D**), and the dose response was compared across 8 short chain acyl-CoA species quantified (**figure 3B, supp 3B-C**). This analysis revealed that HMG-CoA is severely depleted upon acetate withdrawal and increases 10-40 fold with increasing acetate supplementation in *Acly*$^{-/-}$ cells (**figure 3C**). Acetyl-CoA was also sensitive to exogenous acetate, but the concentration changed by only 2-3 fold in the presence or absence of acetate (**figure 3C**). In contrast, malonyl-CoA did not exhibit clear responsivity to acetate in whole cells (**figure 3B**, **supp 3B-C**). Control (*Acly*$^{f/f}$) cells are largely unaffected by acetate supplementation (**figure 3B, supp. 3D**).

To test if the dose-responsive change in HMG-CoA abundance occurs specifically in the cytosol, as might be predicted in *Acly*$^{-/-}$ cells, we performed SILEC-SF to compare acyl-CoA levels specifically in the cytosolic and mitochondrial compartments in response to exogenous acetate. Importantly, the direct extraction and SILEC-SF whole cell data reported consistent trends (**supp. 3B,C,E,F**). Acetyl-CoA levels were not significantly different between low and high acetate in either mitochondrial and cytosolic compartments (**figure 3D**). HMG-CoA, however, responded to acetate dose specifically in the cytosolic and not in the mitochondrial compartment of *Acly*$^{-/-}$ cells (**figure 3D)**. The significant response of cytosolic HMG-CoA to acetate dose was unique amongst a panel of 6 to 7 short chain acyl-CoA species quantified in the cytosol of *Acly*$^{-/-}$ MEF and liver cancer cells (**supp. 3E,F**). Of note, our prior sub-cellular tracing analyses demonstrated a close kinetic relationship between cytosolic acetyl-CoA and HMG-CoA labeling from acetate (Trefely et al., 2019). Together, the data suggest that cytosolic HMG-CoA is highly sensitive to nutritional state, in particular, an abundant supply of carbon sources feeding cytosolic acetyl-CoA pools.

SILEC-SF reveals distinct nuclear acyl-CoA profiles, including enrichment of propionyl-CoA

An understanding of nuclear acyl-CoA levels is of high biological importance since important roles for histone acylation have emerged, but the sources of nuclear acyl-CoAs for regulation of these modifications remain ambiguous (Trefely et al., 2020). Nuclear metabolite quantitation is a particular challenge due, in part, to large nuclear pores through which small molecules can diffuse. To investigate the potential for nuclear-specific acyl-CoA regulation, we performed SILEC-SF using a rapid differential centrifugation protocol to separate nuclear from non-nuclear fractions in normoxia and hypoxia (**figure 4A, supp. 4A-D**; Western blots **supp. 2E**). Although quantification of recovered acyl-CoA abundance was lower in nuclear fractions (2 orders of

bioRxiv preprint doi: https://doi.org/10.1101/2020.07.30.229468; this version posted July 30, 2020. The copyright holder for this preprint (which was not certified by peer review) is the author/funder, who has granted bioRxiv a license to display the preprint in perpetuity. It is made available under aCC-BY-NC 4.0 International license.

magnitude lower than the non-nuclear and whole cell lysate fractions), we were able to quantify 4 major short chain acyl-CoA species in the nuclear fraction (acetyl-CoA, succinyl-CoA, CoASH and propionyl-CoA). The non-nuclear acyl-CoA profile closely reflects that of the whole cell lysate, indicating that the nuclear acyl-CoA pool does not contribute substantially to the whole cell acyl-CoA abundance (**figure 4A, supp. 4A,B**). The wash fraction also reflects the whole cell lysate (**figure 4A, supp. 4A,D**), suggesting that the wash is necessary to remove residual non-nuclear material from the purified nuclear pellet.

Comparison of the acyl-CoA profile of the cytosol (**figure 2D, supp. 2A**) with the nuclear profile (**figure 4A, supp. 4C**) reveals specific differences. Notably, propionyl-CoA is substantially enriched in the nucleus compared to the cytosol. To further investigate this, we examined acetyl-CoA:propionyl-CoA ratio across all sub-cellular fractions (**figure 4B**). Data from the mito/cyto and nuclear/non-nuclear fractionation methods were combined from 3 independent experiments carried out on different days for each method. Importantly, these data are highly consistent across these independent replicates. Acetyl-CoA and propionyl-CoA are equimolar in the nucleus, whereas in the whole cell lysate, cytosolic and non-nuclear fractions, acetyl-CoA is >5-fold more abundant. Notably, the relative quantities of acetyl-CoA and succinyl-CoA are approximately equimolar in nucleus (**supp. 4C**) whereas succinyl-CoA is >4-fold greater than acetyl-CoA in the mitochondria (**supp.2B**). Thus, SILEC-SF reveals distinct and reproducible differences in nuclear acyl-CoA profiles versus other compartments, identifying an enrichment for propionyl-CoA within the nucleus.

Nuclear propionyl-CoA responds to serum withdrawal

Since hypoxia experiments were carried out in the absence of serum, we hypothesized that nuclear propionyl-CoA may accumulate in response to serum limitation. To test this, we incubated cells in the same low nutrient conditions +/- 10% serum for an extended period of time (23 h). Nuclear propionyl-CoA was significantly more abundant under serum starvation (**figure 4D**). This is distinct from the WCL, non-nuclear and wash fractions, in which acetyl-CoA and succinyl-CoA remained the most abundant (**supp. 4E-G**). These data indicate the nucleus exhibits distinct metabolic adaptation to nutrient stress conditions that are not detectable by whole cell measurements, and this is characterized by enrichment of propionyl-CoA.

Isoleucine catabolism contributes to nuclear propionyl-CoA generation

Since propionate is not present in cell culture medium, these data indicate that nuclear propionyl-CoA must be generated from an endogenous source. Pathways for endogenous propionyl-CoA generation are annotated to the mitochondria, where its metabolic fate is the TCA cycle via succinyl-CoA (**figure 4C**), although it may also leave mitochondria via the carnitine shuttle (Trefely et al., 2020). To investigate the metabolic origin of nuclear propionyl-CoA, we first assessed the substrate contribution to total cellular propionyl-CoA by stable isotope tracing of a panel of uniformly ^{13}C-labeled substrates followed by direct extraction of whole cells. Strikingly, isoleucine labeling into propionyl-CoA M3 contributed 50% if the propionyl-CoA pool in the absence of propionate in murine pancreatic adenocarcinoma cells (**supp. 4H**). This accounts for the majority of cellular propionyl-CoA since the tracer was 50% diluted with unlabeled Ile. By contrast, the contribution of Ile to the cellular succinyl-CoA and acetyl-CoA pools was <1% (**supp. 4I,J**), likely reflecting the relatively small contribution of propionyl-CoA to

bioRxiv preprint doi: https://doi.org/10.1101/2020.07.30.229468; this version posted July 30, 2020. The copyright holder for this preprint (which was not certified by peer review) is the author/funder, who has granted bioRxiv a license to display the preprint in perpetuity. It is made available under aCC-BY-NC 4.0 International license.

these much larger pools. Since isoleucine is the dominant substrate for propionyl-CoA generation under these conditions, we tested the potential for Ile to contribute specifically to nuclear propionyl-CoA using sub-cellular kinetic analysis with isotope post-labeling to correct for post-harvest metabolic activity (as described by (Trefely et al., 2019)). Nuclear propionyl-CoA was labeled ~20% by uniformly labeled $^{13}C_6$-isoleucine 50% diluted with unlabeled isoleucine indicating that the propionyl-CoA pool in the nucleus can be substantially derived from Ile **(figure 4E**). Thus, nuclear propionyl-CoA pools are derived at least in part from BCAA catabolism, a pathway that is ascribed to the mitochondria.

Discussion:

SILEC-SF progresses sub-cellular metabolomics

In this study we present SILEC-SF, a rigorous isotope dilution approach to sub-cellular quantitation of acyl-CoAs. This represents a critical tool to directly analyze the mechanistic relationship between acyl-CoA supply and functional outputs of acyl-CoA metabolism including protein acylation and metabolic pathway activity, which are distinct between sub-cellular compartments. Methods to quantify compartmentalized pools are becoming increasingly diverse. Sub-cellular metabolite monitoring using specialized genetically encoded fluorescent metabolite sensors have been applied to a limited set of metabolites, including NAD+, NADH, ATP, glucose, glutamine, lactate and pyruvate (Jaffrey, 2018; Okumoto et al., 2012; Zhang et al., 2018). However, these methods have technical limitations in that they require highly engineered experimental settings, and probes generally do not allow simultaneous monitoring of multiple metabolite species. Mass spectrometry (MS) has the advantage of direct and highly multiplexed analyses. However, sub-cellular analyses have been a major technical challenge in metabolomics due to requirements for sample processing and metabolite extraction. Imaging MS holds great potential but the processing and sensitivity required to achieve robust organelle-specific quantitation for many metabolites is limiting (Niehaus et al.; Thomen et al., 2020). Cellular fractionation can be scaled for appropriate quantitation of a range of biomolecules. We have previously shown that post-harvest metabolism occurs rapidly upon cell harvest and during fractionation (Trefely et al., 2019). The innovation of SILEC-SF mitigate these problems by introducing internal standards as whole cells before fractionation.

SILEC-SF is a flexible approach

SILEC-SF is a flexible approach applicable to a variety of sub-cellular fractionation platforms and adaptable across multiple different classes of metabolites. In this study we applied SILEC-SF to differential centrifugation to achieve simultaneous enrichment of mitochondria and cytosol, and nuclear enrichment. SILEC-SF may, in principle, be applied across multiple platforms for sub-cellular fractionation appropriate for different experimental scenarios such as recently developed immunoprecipitation methods for isolating tagged mitochondria, lysosomes, and peroxisomes for metabolomic analyses (Bayraktar et al., 2019; Chen et al., 2016, 2017; Ray et al., 2020; Wyant et al., 2017; Xiong et al., 2019) and other platforms such as non-aqueous fractionation, generally applied to plant cells (Dietz, 2017; Fly et al., 2015; Krueger et al., 2014) . SILEC labeled cells should be matched as closely as possible to the sample being analysed and be introduced as early as possible in processing. In this study we

bioRxiv preprint doi: https://doi.org/10.1101/2020.07.30.229468; this version posted July 30, 2020. The copyright holder for this preprint (which was not certified by peer review) is the author/funder, who has granted bioRxiv a license to display the preprint in perpetuity. It is made available under aCC-BY-NC 4.0 International license.

utilized a previously described method for generation of SILEC of acyl-CoA metabolites (Basu et al., 2011; Snyder et al., 2014), however, SILEC is not limited to acyl-CoAs or to mammalian cells. The SILEC principle can be extended to other classes of metabolites that can be completely labeled in cell types of interest. For example, we have demonstrated the application of SILEC labeling in mammalian cells for generation of nicotinamide adenine dinucleotide (NAD+/NADH) and nicotinamide adenine dinucleotide phosphate (NADP/NADPH) labeled internal standards (Frederick et al., 2017). Thus SILEC-SF is a principle for rigorous internal standard controls applicable to sub-cellular metabolite quantitation by LC-MS across multiple fractionation platforms.

Application to investigate mechanisms of nutrient sensing and signaling by metabolites

In this study we applied SILEC-SF to the analysis of sub-cellular nutrient responses in mammalian cells. We reveal that cytosolic HMG-CoA is specifically and exquisitely sensitive to exogenous acetate supply in ACLY deficient cells, with a concentration range between 0-3 μM in whole cells. This could potentially limit the activity of the 'rate limiting step' in the mevalonate pathway and target for statin drugs, HMG-CoA reductase (HMGCR, Km for HMG-CoA ~1 µM (Langdon and Counsell, 1976)). Tuning of mevalonate pathway activity could affect availability of important molecules synthesized through this pathway including cholesterol and isoprenoids, implicated in diseases including cancer (Mullen et al., 2016) and insulin resistance (Fazakerley et al., 2018). The sensitivity of the mevalonate pathway to acetate availability may be relevant in the context of the recently approved cholesterol reducing drug bempedoic acid, which acts through ACLY inhibition targeted to the liver (Pinkosky et al., 2016; Ray et al., 2019). These data highlight potential for interactions between dietary factors that affect acetate availability such as alcohol, fiber and fructose consumption (den Besten et al., 2013; Jang et al., 2018; Sarkola et al., 2002; Zhao et al., 2020) and cellular nutrient sensing mechanisms.

Distinct regulation of acyl-CoA metabolism in the nucleus and epigenetic regulation

We make the intriguing observation that propionyl-CoA is enriched in the nucleus relative to other compartments. This is compelling because histone propionylation, which uses propionyl-CoA as a substrate, has emerged as an important regulator of gene transcription. However, levels and sources of propionyl-CoA in the nucleus are unclear (Trefely et al., 2020). We identify isoleucine as a source of nuclear propionyl-CoA. Isoleucine catabolism occurs in the mitochondria and mechanisms of transport to the nucleus are unknown. Interestingly carnitine acetyltransferase (CrAT) has been implicated in provisioning propionyl-CoA for cytosolic fatty acid synthesis (Crown et al., 2015; Green et al., 2015; Wallace et al., 2018), indicating that a similar mechanism involving CrAT may be implicated in the generation of nuclear propionyl-CoA. In future studies, quantitation coupled with genetic manipulation of putative transport mechanisms will be useful to elucidate the spatial organization of metabolic pathways affecting specific organelles including the nucleus and their response to perturbations relevant to disease settings. In particular, analyses of the relationship between acyl-CoA metabolism and a variety of acylation marks affecting histone proteins will shed light on the role of nuclear-specific metabolism in epigenetic regulation.

bioRxiv preprint doi: https://doi.org/10.1101/2020.07.30.229468; this version posted July 30, 2020. The copyright holder for this preprint (which was not certified by peer review) is the author/funder, who has granted bioRxiv a license to display the preprint in perpetuity. It is made available under aCC-BY-NC 4.0 International license.

Methods

TABLE 1: KEY RESOURCES

REAGENT or RESOURCE	SOURCE	IDENTIFIER
Antibodies		
α-Tubulin	Sigma	Cat #T16199
ACSS2	Cell Signaling Technology	Cat #3658, clone D19C66, lot 2
ACLY	Proteintech	Cat #15421-1-AP, lot 00040639
Histone H3	Abcam	Cat #ab1791
Histone H4	Millipore	Cat #05-858
FASN	Cell Signaling Technology	Cat #3189, lot 2
Citrate Synthase	Cell Signaling Technology	Cat #14309, clone D7V8B, lot 1
Lamin A/C	Cell Signaling Technology	Cat #2032
OGDH	Proteintech	Cat #1512-1-AP
SUCLA2	Proteintech	Cat #12627-1-AP
SUCLG1	Proteintech	Cat #14923-1-AP
Chemicals		
Acetyl coenzyme A lithium salt	Sigma-Aldrich	Cat #A2181
DL-β-Hydroxybutyryl coenzyme A lithium salt	Sigma-Aldrich	Cat #H0261
Butyryl coenzyme A lithium salt hydrate	Sigma-Aldrich	Cat #B1508
Coenzyme A trilithium salt	Sigma-Aldrich	Cat #C3019
2-Butenoyl coenzyme A lithium salt	Sigma-Aldrich	Cat #C6146
Glutaryl coenzyme A lithium salt	Sigma-Aldrich	Cat #G9510
DL-3-Hydroxy-3-methylglutaryl coenzyme A sodium salt hydrate	Sigma-Aldrich	Cat #H6132
Isovaleryl coenzyme A lithium salt hydrate	Sigma-Aldrich	Cat #I9381
Malonyl coenzyme A tetralithium salt	Sigma-Aldrich	Cat #63410
n-Propionyl coenzyme A lithium salt	Sigma-Aldrich	Cat #P5397
Succinyl coenzyme A sodium salt	Sigma-Aldrich	Cat #S1129
[13C6,15N2]-Vitamin B5 (calcium pantothenate-13C6,15N2])	Isosciences	Cat #5065
[15N2,13C5]-Glutamine	Cambridge Isotope Laboratories	Cat #CNLM-1275-H-PK
[13C6]-Glucose	Cambridge Isotope Laboratories	Cat #CLM-1396-1
[13C5,15N1]-Valine	Cambridge Isotope Laboratories	Cat #CNLM-422, lot PR-22329
[13C6,15N1]-Leucine	Cambridge Isotope Laboratories	Cat #CNLM-281, lot PR-22831
[13C6]-Isoleucine	Cambridge Isotope Laboratories	Cat #CLM-2248, lot PR-21540
[13C3]-Propionate	Cambridge Isotope Laboratories	Cat #CNLM-1865, lot PR30847/09249SP-1

bioRxiv preprint doi: https://doi.org/10.1101/2020.07.30.229468; this version posted July 30, 2020. The copyright holder for this preprint (which was not certified by peer review) is the author/funder, who has granted bioRxiv a license to display the preprint in perpetuity. It is made available under aCC-BY-NC 4.0 International license.

Experimental Models: Cell Lines		
Acly-/- mouse embryonic fibroblasts (Clone: PC9)	K.E. Wellen Lab	(Zhao et al., 2016)
HepG2	ATCC	Cat. #HB-8065
Murine pancreatic adenocarcinoma (Clone: 2838c3)	B.Z. Stanger Lab	(Li et al., 2018)
Hepa1c17	ATCC	Cat. #CRL-2026
Brown preadipocytes	P. Seale Lab	(Harms et al., 2014)
Murine liver cancer $Acly^{f/f}$ (Clone: D42)	K.E. Wellen Lab	This study
Murine liver cancer $Acly^{-/-}$ (Clone: D42C4)	K.E. Wellen Lab	This study
Software and Algorithms		
Tracefinder v4.1	Thermo Scientific	
FluxFix v1.0		(Trefely et al., 2016)
Graphpad PRISM v8	GraphPad	
Adobe Illustrator software v23.0.1.	Adobe	

Cell Culture

Cells were maintained at 37 °C and 5% CO_2 and passaged every 2–3 days at 80% confluence. All cells were tested and mycoplasma-free. Mouse embryonic fibroblast (MEF) cell lines were cultured in DMEM, high glucose (Thermo Fisher Scientific, Gibco #11965084) with 10% calf serum (Gemini bio-products #100-510, lot C93GOOH). Hepatocellular carcinoma (HepG2) were used at <20 passages and were cultured in DMEM, high glucose with 10% fetal bovine serum (Gemini Biosciences). Murine pancreatic adenocarcinoma cells were cultured in DMEM, high glucose (Thermo Fisher Scientific, Gibco #11965084) with 10% calf serum (Gemini bio-products #100-510, lot C93GOOH). Hepa1c7 cells were cultured in alpha MEM (Thermo Fisher Scientific, Gibco cat. #12561056) with 10% fetal bovine serum (Gemini Biosciences) and penicillin/streptomycin (Thermo Fisher Scientific, Gibco cat. #10378016). Brown adipocytes were prepared from immortalized brown preadipocyte cells (Harms et al., 2014) through induction of differentiation as described previously (Huber et al., 2019).

Liver cancer cell line ($Acly^{f/f}$ clone D42 and $Acly^{-/-}$ clone D42C4) generation

$Acly^{f/f}$ liver cancer cell line (clone D42) was generated from an $Acly^{f/f}$ C57Bl/6J mouse (Zhao et al., 2016) that had liver tumors induced by a single-administration of diethylnitrosamine (25 mg/kg) via intraperitoneal injection at 2 weeks of age and high-fructose diet (Tekland TD.89247) starting at 6 weeks of age. Following euthanasia at 9 months of age, a palpable tumor was excised from the liver avoiding surrounding tissue. The tumor was digested using Miltenyi Liver Dissociation Kit (mouse 130-105-807), and subject to manual dissociation by pipette to form a single cell suspension in DMEM F-12, 10% heat-inactivated FBS, penicillin/streptomycin, and ITS+ Premix Universal Culture Supplement mix (Corning # 354352). The single cell suspension was seeded onto a collagen-coated 6 cm tissue culture dish. Fibroblasts were depleted by differential trypsinization – cells were trypsinized briefly, and detached cells were removed by gentle rinsing with PBS and aspiration. The remaining adherent cells were trypsinized and reseeded using a limiting dilution to derive a proliferating clonal population. After clonal expansion, cells were maintained in DMEM/F-12 with standard 10% calf serum and then DMEM 10% calf serum. $Acly^{-/-}$ liver cancer (clone D42C4) cells were generated from $Acly^{f/f}$ liver cancer cells (clone D42) infected with adenoviral Cre recombinase obtained from the University of Pennsylvania Vector Core. Single cell clonal D42 $Acly^{-/-}$ cell lines

bioRxiv preprint doi: https://doi.org/10.1101/2020.07.30.229468; this version posted July 30, 2020. The copyright holder for this preprint (which was not certified by peer review) is the author/funder, who has granted bioRxiv a license to display the preprint in perpetuity. It is made available under aCC-BY-NC 4.0 International license.

were then generated by limiting dilution and ACLY loss was validated by Western blot. Cell lines were generated while cultured in DMEM/F-12 media (Gibco) supplemented with 10% fetal calf serum and penicillin/streptomycin.

Human heart tissue

Heart tissue was derived from a male organ donor with no history of heart failure, diabetes mellitus or obesity. All study procedures were approved by the University of Pennsylvania Hospital Institutional Review Board, and prospective informed consent for research use of heart tissue was obtained from organ donor next-of-kin. The heart received *in-situ* cold cardioplegia and was placed on wet ice in 4 °C Krebs-Henseleit Buffer. Transmural left ventricular samples, excluding epicardial fat, were cut into 20 mg pieces for and each piece was immediately transferred to a pre-chilled 1 ml Potter-Elvehjem Tissue Grinder (Corning cat. #7725T-1) containing SILEC Hepa1c17 cells in buffer and subjected to fractionation as described below. SILEC Hepa1c17 cells (2.7 E7 cells/sample) were used.

Liver tissue

All animal studies were carried out in accordance with the IACUC guidelines of the University of Pennsylvania. Male C57Bl6 mice fed ad libitum on a chow diet (Laboratory Autoclavable Rodent Diet 5010, LabDiet cat #0001326) were sacrificed at 5 months old by cervical dislocation at 7 am. The frontal lobe was removed to a dish on ice and a 15 mg piece cut and weighed for fractionation. The weighed piece was immediately transferred to a pre-chilled 1 ml Potter-Elvehjem Tissue Grinder (Corning cat. #7725T-1) containing SILEC HepG2 cells in fractionation buffer prepared as described below. The equivalent of 1 10cm dish of 80% confluent SILEC HepG2 cells (~1E7 cells) was used for each sample. Each n represents a different mouse.

SILEC cell preparation

SILEC labeling of cell lines at an efficiency of >99% across all measurable acyl-CoA species was achieved through the passaging of cells in $^{15}N_1{}^{13}C_3$-pantothenate (Vitamin B5) for at least 9 passages as previously described (Basu et al., 2011). SILEC media was prepared by the addition $^{15}N_1{}^{13}C_3$-pantothenate (Isosciences) (1 mg/L) to custom pantothenate free DMEM (Gibco, Thermo Fisher Scientific) containing 25 mM glucose and 4 mM glutamine with all other components at concentrations according to the standard formulation (Dulbecco and Freeman, 1959). Charcoal:dextran stripped fetal bovine serum (Gemini Biosciences cat. #100-199) was added to 10% (v/v). Labeling efficiency was tested by isotopologue enrichment analysis with comparison to unlabeled control cells. Each batch of charcoal:dextran stripped fetal bovine serum was tested for sufficient labeling efficiency after 3 passages since this can vary from batch to batch(Snyder et al., 2014).

SILEC labeling was performed in multiple cell lines to match experimental cells. To reduce potential for interference from the small fraction of unlabeled acyl-CoA in SILEC cells, and the expense of each experiment, SILEC internal standard was added at lower abundance than experimental cells. However, SILEC internal standard abundance was maintained within the same order of magnitude for analytical robustness. Thus, one third to half the amount of SILEC cells were used for each experimental cell sample.

bioRxiv preprint doi: https://doi.org/10.1101/2020.07.30.229468; this version posted July 30, 2020. The copyright holder for this preprint (which was not certified by peer review) is the author/funder, who has granted bioRxiv a license to display the preprint in perpetuity. It is made available under aCC-BY-NC 4.0 International license.

Mitochondria and cytosol isolation

Mitochondrial and cytosolic fractions were isolated by classical differential centrifugation protocol (Clayton and Shadel, 2014; Frezza et al., 2007), with adaptations for speed and purity (illustrated in **supp. 1D**). SILEC cells matched to the experimental cell type were harvested first. Media was poured from SILEC cell dishes into a waste container and cells were placed on ice at a 45° angle and residual media drained and aspirated completely. Dishes were laid flat on ice and 1 ml ice-cold buffer (210 mM mannitol, 70 mM sucrose, 5 mM Tris–HCl (pH 7.5), 1 mM EDTA (pH 8), adjusted to pH 7.5) added to each dish. Cells were scraped into the buffer, mixed against the plate with a P1000 pipette 6 times to break up cell clumps and combined in a 50 ml tube on ice. The volume was made up to >n+1 ml with buffer (1 ml required per sample). A homogenous cell suspension was made by mixing against the wall of the tube 6 times using a 10 ml pipette immediately before addition to experimental dishes.

For brown adipocytes each sample was a confluent 10 cm dish (~4E5 cells/sample), for *Acly*-/- mouse embryonic fibroblasts each sample was a 80% confluent 15 cm dish (~0.6E5 cells/sample), for HepG2 cells each sample was 1 10 cm dish at 80% confluence (~1E7 cells/sample). Media was removed from experimental cells in the same manner as for the SILEC cells and 1 ml of ice-cold homogenous SILEC cell suspension was added to each. Cells were scraped into the SILEC suspension and transferred to a pre-chilled 1 ml Potter-Elvehjem Tissue Grinder (Corning cat. #7725T-1) in a beaker of ice and water. For standard curve samples, SILEC cell suspension without experimental cells was transferred directly to tissue grinder. Cells were lysed by stroking with the pestle attached to an overhead stirrer (SOS20, Southwest Science) operated at 1,600 rpm. Optimal stroke number was determined for each cell line (10 strokes for Hepa1c17 cells, 15 strokes for HepG2 and liver cancer cell lines (D42/D42C4), 20 strokes for heart tissue and brown adipocytes, 30 strokes for MEF cells) by assessing the purity and integrity of mitochondria and cytosol by Western blot and the intensity of acyl-CoA signal within each compartment across a range up to 60 strokes. Homogenate was transferred to 1.5 ml tubes on ice. For WCL analysis, a 100 µl aliquot of homogenate (representing 10% of the total sample) was removed and quenched in 1 ml ice-cold 10% TCA (Sigma cat. #T6399) in water. Homogenate was centrifuged at 1,300 ×*g* from 10 min at 4 °C and supernatant was transferred to a new pre-chilled 1.5 ml tube. The 'heavy debris' pellet was quenched by resuspension in 1 ml 10% TCA and the supernatant was centrifuged at 10,000 ×*g* for 20 min at 4 °C to pellet mitochondria. The supernatant (the cytosolic fraction) was quenched by transferal to a new 1.5 ml tube containing 0.25 ml of 50% (w/v) TCA in water to make a final concentration of 10% TCA. Residual cytosolic fraction was carefully removed from the mitochondrial pellet with P200 pipette, and the pellet was quenched by resuspension in 1 ml 10% (w/v) TCA in water. Samples were stored at -80 °C before thawing on ice for acyl-CoA processing, or directly processed.

Nuclear isolation

Nuclear isolation was achieved by detergent assisted hypoosmotic lysis and differential centrifugation (illustrated in **supp. 1D**). SILEC cells matched to the experimental cell type were harvested before experimental cells. Media was poured from SILEC cell dishes into a waste container, and cells were placed on ice at a 45° angle and residual media drained and aspirated

bioRxiv preprint doi: https://doi.org/10.1101/2020.07.30.229468; this version posted July 30, 2020. The copyright holder for this preprint (which was not certified by peer review) is the author/funder, who has granted bioRxiv a license to display the preprint in perpetuity. It is made available under aCC-BY-NC 4.0 International license.

completely. Dishes were laid flat on ice and 0.5 ml ice-cold lysis buffer (250 mM sucrose, 15 mM Tris–HCl (pH 7.5), 60 mM KCl, 15 mM NaCl, 5 mM $MgCl_2$, 1 mM $CaCl_2$ adjusted to pH 7.4) added to each dish. SILEC cells were scraped into the buffer, cell clumps were broken up by pipetting up and down against the plate 4 times with a P1000. Cells were then combined in a 15 ml tube on ice. The volume was made up to > 0.5*n ml (0.5 ml required per sample) with buffer and kept on ice. Immediately before addition to experimental dishes, NP-40 (1% v/v in lysis buffer) was added to achieve a final concentration of 0.1% (v/v) and the cell suspension was homogenized by mixing by laminar flow against the wall of the 15 ml tube 4 times with a 5 ml pipette with care taken to avoid frothing. NP-40 addition was delayed to coordinate detergent lysis of SILEC cells with experimental cells.

Media was removed from experimental cells in the same manner as for the SILEC cells and 0.5 ml of ice-cold homogenous SILEC cell suspension was added to each dish/sample. Cells were scraped into the SILEC suspension, mixed against the plate with a P1000 pipette 4 times to break up cell clumps and transferred to a 1.5 ml tube on ice. For WCL analysis, 50 µl (representing 10% of the total sample) was removed after homogenization and quenched in 1 ml ice-cold 10% TCA in water. Nuclei were pelleted by centrifugation at 600 ×*g* for 5 min at 4 °C. The supernatant (the 'non-nuclear' fraction) was quenched by transferal to a new 1.5 ml tube containing 0.125 ml of 50% (w/v) TCA in water to make a final concentration of 10% TCA. The nuclear pellet was washed by the addition of 0.5 ml lysis buffer without NP-40 and re-centrifuged at 600 ×*g* for 5 min at 4 °C. The supernatant (the 'wash' fraction) was quenched by transferal to a new 1.5 ml tube containing 0.125 ml of 50% (w/v) TCA in water to make a final concentration of 10% TCA. Residual wash was carefully removed from the nuclear pellet with a P200 pipette, and the nuclear pellet was quenched by the resuspension in 1 ml 10% w/v TCA in water.

Standard curve generation

Separate standard curves were generated for each sub-cellular fraction. Equal aliquots of SILEC internal standard cells were fractionated in the absence of experimental unlabeled cells and known quantities of unlabeled standards were added before extraction (**supp. 1A**). 6-point standard curves (standard 0 to standard 5) were generated for each fraction by dilution from a stock mixture of unlabeled acyl-CoA standards. The stock mixture was dissolved in 10% TCA in water according to **Table 2** and aliquots were frozen at -80 and thawed once at use. Serial 3-fold dilutions were made from standard 5 stock in 10% TCA in water and each dilution was added in a volume of 100 µl to the appropriate samples containing SILEC internal standard. The concentration of standard 5 (the highest standard) stock was adjusted to suit metabolite abundance in different samples. For most cell samples standard 5 stock was a 50x dilution of the original stock mixture (mitochondrial and nuclear fractions used a 250x dilution). For most tissue samples, standard 5 stock was a 20x dilution of stock mixture (mitochondrial and nuclear fractions used a 100x dilution).

Table 2: Acyl-CoA standard mixture

Unlabeled standard	Concentration (pmol/100 µl)
Acetyl-CoA	5000
BHB-CoA	500

bioRxiv preprint doi: https://doi.org/10.1101/2020.07.30.229468; this version posted July 30, 2020. The copyright holder for this preprint (which was not certified by peer review) is the author/funder, who has granted bioRxiv a license to display the preprint in perpetuity. It is made available under aCC-BY-NC 4.0 International license.

Butyryl-CoA	500
CoASH	500
Crotonoyl-CoA (2-butenoyl-CoA)	500
Glutaryl-CoA	500
HMG-CoA	500
Isovaleryl-CoA	500
Malonyl-CoA	500
Propionyl-CoA	500
Succinyl-CoA	5000

Normalization

Data were normalized to cell counts from an extra replicate cell dish for each condition. Cells were trypsinzed and total cell number and volume was determined by Coulter counter (Coulter). For tissue samples, tissue pieces were weighed on a balance to +/- 0.01 mg before fractionation and data was normalized to mass for each sample.

Whole cell direct extraction

Media was poured from dishes into a waste container and cells were placed on ice at a 45° angle and residual media aspirated completely. Dishes were laid flat on ice and 1 ml 10% TCA in water was added. Internal standard extracted from yeast grown in $^{15}N_1{}^{13}C_3$-pantothenate as previously described (Snyder et al., 2015) was added (100 µl/sample). Cells were scraped into the TCA and transferred to 1.5 ml tubes on ice then either processed directly or stored at -80 °C. Standard curves were generated in parallel with equal aliquots of internal standard in 10% TCA in water.

Stable isotope tracing in whole cells

Murine pancreatic adenocarcinoma cells were seeded at 0.4 E6 cells/well in a 6-well plate 2 days before treatment. At 80% confluent, cells were preincubated in serum-free DMEM (Thermo Fisher Scientific, Gibco #11965084) for 8 hours. Tracing media was prepared using DMEM base lacking glucose or glutamine (Thermo-Fisher scientific, Gibco cat. #A1443001). Glucose was replaced at (4.5 g/L), and glutamine at (584 mg/L) and additional isoleucine (105 mg/L), valine (94 mg/L) and leucine (105 mg/L) were added. Except for the targeted experimental tracer ($U^{13}C$, see **Table 1**), all additives were unlabeled. Total substrate concentrations were equal across all samples except propionate, which was added only to the $U^{13}C$-propionate tracing samples at 1 mM. Whole cell direct extraction was performed after incubation in tracing media at 37 °C and 5% CO_2 for 18 hours.

Sub-cellular stable isotope tracing with post-labeling

Murine pancreatic ductal adenocarcinoma cells were incubated with $U^{13}C$-isoleucine tracer before fractionation as described above. Fractionation with post-labeling was carried out as previously described (Trefely et al., 2019) with the addition of $U^{13}C$-isoleucine (525 mg/L) and unlabeled isoleucine (525 mg/L) to fractionation buffer.

bioRxiv preprint doi: https://doi.org/10.1101/2020.07.30.229468; this version posted July 30, 2020. The copyright holder for this preprint (which was not certified by peer review) is the author/funder, who has granted bioRxiv a license to display the preprint in perpetuity. It is made available under aCC-BY-NC 4.0 International license.

Acyl-CoA sample processing

Samples were thawed and kept on ice throughout processing. Cell and fraction samples in 10% (w/v) trichloroacetic acid (Sigma cat. #T6399) in water were sonicated for 12 × 0.5 s pulses, protein was pelleted by centrifugation at 17,000 ×*g* from 10 min at 4 °C. The supernatant was purified by solid-phase extraction using Oasis HLB 1cc (30 mg) SPE columns (Waters). Columns were washed with 1 mL methanol, equilibrated with 1 mL water, loaded with supernatant, desalted with 1 mL water, and eluted with 1 mL methanol containing 25 mM ammonium acetate. The purified extracts were evaporated to dryness under nitrogen then resuspended in 55 µl 5% (w/v) 5-sulfosalicylic acid in water.

Acyl-CoA analysis by LC-MS

Acyl-CoAs were measured by liquid chromatography-high resolution mass spectrometry. Briefly, 5–10 µl of purified samples in 5% SSA were analyzed by injection of an Ultimate 3000 Quaternary UHPLC coupled to a Q Exactive Plus (Thermo Scientific) mass spectrometer in positive ESI mode using the settings described previously (Frey et al., 2016). Quantification of acyl-CoAs was via their MS2 fragments and the targeted masses used for isotopologue analysis are indicated in **Table 3**. Data were integrated using Tracefinder v4.1 (Thermo Scientific) software. Isotopic enrichment in tracing experiments was calculated by normalization to unlabeled control samples using the FluxFix calculator (Trefely et al., 2016).

Western blotting

Western blotting was performed using mini gel tank system (Life Biotechnologies) with 4–12% gradient Bis-Tris gels (NuPage, Invitrogen cat. #NP0335) and 0.45 µm pore size nitrocellulose membranes (BioRad cat. #1620115) with antibody (see **Table 1**) incubations according to the manufacturer's instructions. An Odyssey CLx imaging system with Image Studio v2.0.38 software (LI-COR Biosciences) was used to acquire images which were exported as TIFF files then cropped and arranged using Adobe Illustrator software v23.0.1.

Graphing and statistical analyses

Data presented are shown either of mean ± standard deviation or, for curve fits, mean ± 95% confidence intervals. Graphpad Prism software (v.8) was used for graphing and statistical analysis. For comparison between two groups, datasets were analyzed by two-tailed Student's *t*-test with Welch's correction and statistical significance defined as $p < 0.05$ (*), $p < 0.01$ (**), $p < 0.001$ (***), $p < 0.0001$ (****).

bioRxiv preprint doi: https://doi.org/10.1101/2020.07.30.229468; this version posted July 30, 2020. The copyright holder for this preprint (which was not certified by peer review) is the author/funder, who has granted bioRxiv a license to display the preprint in perpetuity. It is made available under aCC-BY-NC 4.0 International license.

Table 3: Acyl-CoA Masses

Isotopologue	Precursor Formula [M]	Precursor Ion [M+H]+	Product Ion [M+H-507]+
Acetyl-CoA-M0	C23H38N7O17P3S	810.1331	303.1373
Acetyl-CoA ISTD	[13]C3C20H38[15]N1N6O17P3S	814.1402	307.1444
Acetyl-CoA-M1	[13]C1C22H38N7O17P3S	811.1364	304.1407
Acetyl-CoA-M2	[13]C2C21H38N7O17P3S	812.1398	305.1440
Acetyl-CoA-M3	[13]C3C20H38N7O17P3S	813.1431	306.1474
Acetyl-CoA-M4	[13]C4C19H38N7O17P3S	814.1465	307.1507
Acetyl-CoA-M5	[13]C5C18H38N7O17P3S	815.1498	308.1541
BH(I)B-CoA	C25H42N7O18P3S	854.1593	347.1635
BH(I)B-CoA ISTD	[13]C3C22H42[15]N1N6O18P3S	858.1664	351.1706
CoASH	C21H36N7O16P3S	768.1225	-
CoASH ISTD	[13]C3C18H36[15]N1N6O16P3S	772.1296	-
Crotonoyl-CoA	C25H40N7O17P3S	836.1487	329.1530
Crotonoyl-CoA ISTD	[13]C3C22H40[15]N1N6O17P3S	840.1558	333.1601
Glutaryl-CoA	C26H42N7O19P3S	882.1542	375.1584
Glutaryl-CoA ISTD	[13]C3C23H42[15]N1N6O19P3S	886.1613	379.1655
HMG-CoA	C27H44N7O20P3S	912.1647	405.1690
HMG-CoA ISTD	[13]C3C24H44[15]N1N6O20P3S	916.1718	409.1761
(iso)Butyryl-CoA	C25H42N7O17P3S	838.1644	331.1686
(iso)Butyryl-CoA ISTD	[13]C3C22H42[15]N1N6O17P3S	842.1715	335.1757
(iso)Valeryl-CoA	C26H44N7O17P3S	852.1800	345.1843
(iso)Valeryl-CoA ISTD	[13]C3C23H44[15]N1N6O17P3S	856.1871	349.1914
Propionyl-CoA-M0	C24H40N7O17P3S	824.1487	317.1530
Propionyl-CoA ISTD	[13]C3C21H40[15]N1N6O17P3S	828.1558	321.1601
Propionyl-CoA-M1	[13]C1C23H40N7O17P3S	825.1521	318.1563
Propionyl-CoA-M2	[13]C2C22H40N7O17P3S	826.1554	319.1488
Propionyl-CoA-M3	[13]C3C20H40N7O17P3S	827.1588	320.1521
Propionyl-CoA-M4	[13]C4C19H40N7O17P3S	828.1621	321.1555
Propionyl-CoA-M5	[13]C5C18H40N7O17P3S	829.1655	322.1564
Succinyl-CoA-M0	C25H40N7O19P3S	868.1385	361.1428
Succinyl-CoA ISTD	[13]C3C22H40[15]N1N6O19P3S	872.1456	365.1499
Succinyl-CoA-M1	[13]C1C24H40N7O19P3S	869.1419	362.1461
Succinyl-CoA-M2	[13]C2C23H40N7O19P3S	870.1452	363.1495
Succinyl-CoA-M3	[13]C3C22H40N7O19P3S	871.1486	364.1528
Succinyl-CoA-M4	[13]C4C21H40N7O19P3S	872.1520	365.1562
Succinyl-CoA-M5	[13]C5C20H40N7O19P3S	873.1553	366.1596
Succinyl-CoA-M6	[13]C6C19H40N7O19P3S	874.1587	367.1629
Succinyl-CoA-M7	[13]C7C18H40N7O19P3S	875.1620	368.1663

*3-hydroxymethylglutaryl-CoA (HMG-CoA)

*3-hydroxybutyrate-CoA/3-hydroxyisobutyrate-CoA (BH(I)B-CoA)

ISTD = internal standard

CoASH was quantified using MS1 Precursor ion

bioRxiv preprint doi: https://doi.org/10.1101/2020.07.30.229468; this version posted July 30, 2020. The copyright holder for this preprint (which was not certified by peer review) is the author/funder, who has granted bioRxiv a license to display the preprint in perpetuity. It is made available under aCC-BY-NC 4.0 International license.

Author contributions

ST, NWS, and KEW conceptualized the study and designed experiments. ST prepared figures and wrote the manuscript. NWS and KEW edited the manuscript. ST performed the majority of the experiments and data analysis. JL and KH performed experiments and analysis. JS, EVK, MD, HJ and AB performed metabolite extraction and analysis. CL and MN performed tracing experiments. LI and SZ generated D42 and D42C4 liver cancer cell lines. JER and KCB procured heart samples. JB-S supported KH and provided useful discussion. CM provided valuable advice and support with mass spectrometry. All authors read and provided feedback on manuscript and figures.

Acknowledgements

NWS was supported by R01GM132261 and P30ES013508. KEW is supported by R01CA228339, R01DK116005, and R01CA174761. ST was supported by the American Diabetes Association through post-doctoral fellowship 1-18-PDF-144. KH and JB-S were supported by the Austrian Science Fund grants FWF W1226 and FWF P27108. CDL is supported by NIH T32 GM07170. LI was supported by T32 GM-07229. SZ was supported by F99CA222741.

bioRxiv preprint doi: https://doi.org/10.1101/2020.07.30.229468; this version posted July 30, 2020. The copyright holder for this preprint (which was not certified by peer review) is the author/funder, who has granted bioRxiv a license to display the preprint in perpetuity. It is made available under aCC-BY-NC 4.0 International license.

References

Basu, S.S., Mesaros, C., Gelhaus, S.L., and Blair, I.A. (2011). Stable Isotope Labeling by Essential Nutrients in Cell Culture for Preparation of Labeled Coenzyme A and Its Thioesters. Anal. Chem. *83*, 1363–1369.

Bayraktar, E.C., Baudrier, L., Özerdem, C., Lewis, C.A., Chan, S.H., Kunchok, T., Abu-Remaileh, M., Cangelosi, A.L., Sabatini, D.M., Birsoy, K., et al. (2019). MITO-Tag Mice enable rapid isolation and multimodal profiling of mitochondria from specific cell types in vivo. Proc. Natl. Acad. Sci. *116*, 303–312.

Bedi, K.C., Snyder, N.W., Brandimarto, J., Aziz, M., Mesaros, C., Worth, A.J., Wang, L.L., Javaheri, A., Blair, I.A., Margulies, K.B., et al. (2016). Evidence for Intramyocardial Disruption of Lipid Metabolism and Increased Myocardial Ketone Utilization in Advanced Human Heart Failure. Circulation *133*, 706–716.

den Besten, G., van Eunen, K., Groen, A.K., Venema, K., Reijngoud, D.-J., and Bakker, B.M. (2013). The role of short-chain fatty acids in the interplay between diet, gut microbiota, and host energy metabolism. J. Lipid Res. *54*, 2325–2340.

Chen, W.W., Freinkman, E., Wang, T., Birsoy, K., and Sabatini, D.M. (2016). Absolute Quantification of Matrix Metabolites Reveals the Dynamics of Mitochondrial Metabolism. Cell *166*, 1324-1337.e11.

Chen, W.W., Freinkman, E., and Sabatini, D.M. (2017). Rapid immunopurification of mitochondria for metabolite profiling and absolute quantification of matrix metabolites. Nat. Protoc. *12*, 2215–2231.

Ciccimaro, E., and Blair, I.A. (2010). Stable-isotope dilution LC-MS for quantitative biomarker analysis. Bioanalysis *2*, 311–341.

Clayton, D.A., and Shadel, G.S. (2014). Purification of mitochondria by sucrose step density gradient centrifugation. Cold Spring Harb. Protoc. *2014*, pdb.prot080028.

Cluntun, A.A., Huang, H., Dai, L., Liu, X., Zhao, Y., and Locasale, J.W. (2015). The rate of glycolysis quantitatively mediates specific histone acetylation sites. Cancer Metab.

Crown, S.B., Marze, N., and Antoniewicz, M.R. (2015). Catabolism of Branched Chain Amino Acids Contributes Significantly to Synthesis of Odd-Chain and Even-Chain Fatty Acids in 3T3-L1 Adipocytes. PLoS One *10*, e0145850.

Dietz, K.-J. (2017). Subcellular Metabolomics: The Choice of Method Depends on the Aim of the Study. J. Exp. Bot. *68*, 5695–5698.

Dulbecco, R., and Freeman, G. (1959). Plaque production by the polyoma virus. Virology *8*, 396–397.

Fazakerley, D.J., Chaudhuri, R., Yang, P., Maghzal, G.J., Thomas, K.C., Krycer, J.R., Humphrey, S.J., Parker, B.L., Fisher-Wellman, K.H., Meoli, C.C., et al. (2018). Mitochondrial CoQ deficiency is a common driver of mitochondrial oxidants and insulin resistance. Elife *7*.

Fly, R., Lloyd, J., Krueger, S., Fernie, A., and van der Merwe, M.J. (2015). Improvements to defi ne mitochondrial metabolomics using nonaqueous fractionation. Methods Mol. Biol. *1305*, 197–210.

Frederick, D.W., Trefely, S., Buas, A., Goodspeed, J., Singh, J., Mesaros, C., Baur, J.A., and Snyder, N.W. (2017). Stable isotope labeling by essential nutrients in cell culture (SILEC) for accurate measurement of nicotinamide adenine dinucleotide metabolism. Analyst *142*, 4431–

bioRxiv preprint doi: https://doi.org/10.1101/2020.07.30.229468; this version posted July 30, 2020. The copyright holder for this preprint (which was not certified by peer review) is the author/funder, who has granted bioRxiv a license to display the preprint in perpetuity. It is made available under aCC-BY-NC 4.0 International license.

4437.
Frey, A.J., Feldman, D.R., Trefely, S., Worth, A.J., Basu, S.S., and Snyder, N.W. (2016). LC-quadrupole/Orbitrap high-resolution mass spectrometry enables stable isotope-resolved simultaneous quantification and (13)C-isotopic labeling of acyl-coenzyme A thioesters. Anal. Bioanal. Chem. *408*, 3651–3658.
Frezza, C., Cipolat, S., and Scorrano, L. (2007). Organelle isolation: functional mitochondria from mouse liver, muscle and cultured fibroblasts. Nat. Protoc. *2*, 287–295.
Green, C.R., Wallace, M., Divakaruni, A.S., Phillips, S.A., Murphy, A.N., Ciaraldi, T.P., and Metallo, C.M. (2015). Branched-chain amino acid catabolism fuels adipocyte differentiation and lipogenesis. Nat. Chem. Biol. *12*, 15–21.
Guilbault, G.G., and Hjelm, M. (1989). Nomenclature for automated and mechanised analysis (Recommendations 1989). Pure Appl. Chem. *61*, 1657–1664.
Harms, M.J., Ishibashi, J., Wang, W., Lim, H.W., Goyama, S., Sato, T., Kurokawa, M., Won, K.J., and Seale, P. (2014). Prdm16 is required for the maintenance of brown adipocyte identity and function in adult mice. Cell Metab. *19*, 593–604.
Huber, K., Hofer, D.C., Trefely, S., Pelzmann, H.J., Madreiter-Sokolowski, C., Duta-Mare, M., Schlager, S., Trausinger, G., Stryeck, S., Graier, W.F., et al. (2019). N-acetylaspartate pathway is nutrient responsive and coordinates lipid and energy metabolism in brown adipocytes. Biochim. Biophys. Acta - Mol. Cell Res. *1866*, 337–348.
Jaffrey, S.R. (2018). RNA-Based Fluorescent Biosensors for Detecting Metabolites in vitro and in Living Cells. In Advances in Pharmacology, (Academic Press Inc.), pp. 187–203.
Jang, C., Hui, S., Lu, W., Cowan, A.J., Morscher, R.J., Lee, G., Liu, W., Tesz, G.J., Birnbaum, M.J., and Rabinowitz, J.D. (2018). The Small Intestine Converts Dietary Fructose into Glucose and Organic Acids. Cell Metab. *27*, 351-361.e3.
Krueger, S., Steinhauser, D., Lisec, J., and Giavalisco, P. (2014). Analysis of subcellular metabolite distributions within arabidopsis thaliana leaf tissue: A primer for subcellular metabolomics. Methods Mol. Biol. *1062*, 575–596.
Langdon, R.B., and Counsell, R.E. (1976). Determination of the michaelis-menten constant for beta-hydroxy-beta-methylglutaryl coenzyme A reductase. Demonstration of a substrate affinity 10-fold greater than previously reported. J. Biol. Chem. *251*, 5820–5823.
Lee, J.V., Carrer, A., Shah, S., Snyder, N.W., Wei, S., Venneti, S., Worth, A.J., Yuan, Z.-F., Lim, H.-W., Liu, S., et al. (2014). Akt-Dependent Metabolic Reprogramming Regulates Tumor Cell Histone Acetylation. Cell Metab. *20*, 306–319.
Li, J., Byrne, K.T., Yan, F., Yamazoe, T., Chen, Z., Baslan, T., Richman, L.P., Lin, J.H., Sun, Y.H., Rech, A.J., et al. (2018). Tumor Cell-Intrinsic Factors Underlie Heterogeneity of Immune Cell Infiltration and Response to Immunotherapy. Immunity *49*, 178-193.e7.
Li, X., Yu, W., Qian, X., Xia, Y., Zheng, Y., Lee, J.-H.H., Li, W., Lyu, J., Rao, G., Zhang, X., et al. (2017). Nucleus-Translocated ACSS2 Promotes Gene Transcription for Lysosomal Biogenesis and Autophagy. Mol. Cell *66*, 684-697.e9.
Lu, W., Su, X., Klein, M.S., Lewis, I.A., Fiehn, O., and Rabinowitz, J.D. (2017). Metabolite Measurement: Pitfalls to Avoid and Practices to Follow. Annu. Rev. Biochem. *86*, 277–304.
Mann, M. (2006). Functional and quantitative proteomics using SILAC. Nat. Rev. Mol. Cell Biol.
Metallo, C.M., Gameiro, P.A., Bell, E.L., Mattaini, K.R., Yang, J., Hiller, K., Jewell, C.M., Johnson, Z.R., Irvine, D.J., Guarente, L., et al. (2011). Reductive glutamine metabolism by IDH1 mediates

bioRxiv preprint doi: https://doi.org/10.1101/2020.07.30.229468; this version posted July 30, 2020. The copyright holder for this preprint (which was not certified by peer review) is the author/funder, who has granted bioRxiv a license to display the preprint in perpetuity. It is made available under aCC-BY-NC 4.0 International license.

lipogenesis under hypoxia. Nature *481*, 380–384.
Mews, P., Donahue, G., Drake, A.M., Luczak, V., Abel, T., and Berger, S.L. (2017). Acetyl-CoA synthetase regulates histone acetylation and hippocampal memory. *546*, 381–386.
Mullen, P.J., Yu, R., Longo, J., Archer, M.C., and Penn, L.Z. (2016). The interplay between cell signalling and the mevalonate pathway in cancer. Nat. Rev. Cancer *16*, 718–731.
Niehaus, M., Soltwisch, J., Belov, M.E., and Dreisewerd, K. Transmission-mode MALDI-2 mass spectrometry imaging of cells and tissues at subcellular resolution. Nat. Methods.
Okumoto, S., Jones, A., and Frommer, W.B. (2012). Quantitative Imaging with Fluorescent Biosensors. Annu. Rev. Plant Biol. *63*, 663–706.
Ong, S.E. (2012). The expanding field of SILAC. Anal. Bioanal. Chem. *404*, 967–976.
Pinkosky, S.L., Newton, R.S., Day, E.A., Ford, R.J., Lhotak, S., Austin, R.C., Birch, C.M., Smith, B.K., Filippov, S., Groot, P.H.E., et al. (2016). Liver-specific ATP-citrate lyase inhibition by bempedoic acid decreases LDL-C and attenuates atherosclerosis. Nat. Commun. *7*.
Ray, G.J., Boydston, E.A., Shortt, E., Wyant, G.A., Lourido, S., Chen, W.W., and Sabatini, D.M. (2020). A PEROXO-Tag enables rapid isolation of peroxisomes from human cells. BioRxiv 2020.03.10.984948.
Ray, K.K., Bays, H.E., Catapano, A.L., Lalwani, N.D., Bloedon, L.A.T., Sterling, L.R., Robinson, P.L., and Ballantyne, C.M. (2019). Safety and efficacy of bempedoic acid to reduce LDL cholesterol. N. Engl. J. Med. *380*, 1022–1032.
Sadhukhan, S., Liu, X., Ryu, D., Nelson, O.D., Stupinski, J.A., Li, Z., Chen, W., Zhang, S., Weiss, R.S., Locasale, J.W., et al. (2016). Metabolomics-assisted proteomics identifies succinylation and SIRT5 as important regulators of cardiac function. Proc. Natl. Acad. Sci. *113*, 4320–4325.
Sarkola, T., Iles, M.R., Kohlenberg-Mueller, K., and Eriksson, C.J.P. (2002). Ethanol, Acetaldehyde, Acetate, and Lactate Levels After Alcohol Intake in White Men and Women: Effect of 4-Methylpyrazole. Alcohol. Clin. Exp. Res.
Simithy, J., Sidoli, S., Yuan, Z.-F., Coradin, M., Bhanu, N. V., Marchione, D.M., Klein, B.J., Bazilevsky, G.A., McCullough, C.E., Magin, R.S., et al. (2017). Characterization of histone acylations links chromatin modifications with metabolism. Nat. Commun. *8*, 1141.
Sivanand, S., Rhoades, S., Jiang, Q., Lee, J. V., Benci, J., Zhang, J., Yuan, S., Viney, I., Zhao, S., Carrer, A., et al. (2017). Nuclear Acetyl-CoA Production by ACLY Promotes Homologous Recombination. Mol. Cell *67*, 252-265.e6.
Sivanand, S., Viney, I., and Wellen, K.E. (2018). Spatiotemporal Control of Acetyl-CoA Metabolism in Chromatin Regulation. Trends Biochem. Sci. *43*, 61–74.
Snyder, N.W., Basu, S.S., Zhou, Z., Worth, A.J., and Blair, I.A. (2014). Stable isotope dilution liquid chromatography/mass spectrometry analysis of cellular and tissue medium- and long-chain acyl-coenzyme A thioesters. Rapid Commun. Mass Spectrom. *28*, 1840–1848.
Snyder, N.W., Tombline, G., Worth, A.J., Parry, R.C., Silvers, J.A., Gillespie, K.P., Basu, S.S., Millen, J., Goldfarb, D.S., and Blair, I.A. (2015). Production of stable isotope-labeled acyl-coenzyme A thioesters by yeast stable isotope labeling by essential nutrients in cell culture. Anal. Biochem. *474C*, 59–65.
Sun, R.C., Dukhande, V. V., Zhou, Z., Young, L.E.A., Emanuelle, S., Brainson, C.F., and Gentry, M.S. (2019). Nuclear Glycogenolysis Modulates Histone Acetylation in Human Non-Small Cell Lung Cancers. Cell Metab. *30*, 903-916.e7.
Sutendra, G., Kinnaird, A., Dromparis, P., Paulin, R., Stenson, T.H.H., Haromy, A., Hashimoto, K.,

bioRxiv preprint doi: https://doi.org/10.1101/2020.07.30.229468; this version posted July 30, 2020. The copyright holder for this preprint (which was not certified by peer review) is the author/funder, who has granted bioRxiv a license to display the preprint in perpetuity. It is made available under aCC-BY-NC 4.0 International license.

Zhang, N., Flaim, E., and Michelakis, E.D.D. (2014). A Nuclear Pyruvate Dehydrogenase Complex Is Important for the Generation of Acetyl-CoA and Histone Acetylation. Cell *158*, 84–97.

Thomen, A., Najafinobar, N., Penen, F., Kay, E., Upadhyay, P.P., Li, X., Phan, N.T.N., Malmberg, P., Klarqvist, M., Andersson, S., et al. (2020). Subcellular Mass Spectrometry Imaging and Absolute Quantitative Analysis across Organelles. ACS Nano.

Trefely, S., Ashwell, P., and Snyder, N.W. (2016). FluxFix: automatic isotopologue normalization for metabolic tracer analysis. BMC Bioinformatics *17*, 485.

Trefely, S., Liu, J., Huber, K., Doan, M.T., Jiang, H., Singh, J., von Krusenstiern, E., Bostwick, A., Xu, P., Bogner-Strauss, J.G., et al. (2019). Subcellular metabolic pathway kinetics are revealed by correcting for artifactual post harvest metabolism. Mol. Metab. *30*, 61–71.

Trefely, S., Lovell, C.D., Snyder, N.W., and Wellen, K.E. (2020). Compartmentalised acyl-CoA metabolism and roles in chromatin regulation. Mol. Metab. 100941.

Wallace, M., Green, C.R., Roberts, L.S., Lee, Y.M., McCarville, J.L., Sanchez-Gurmaches, J., Meurs, N., Gengatharan, J.M., Hover, J.D., Phillips, S.A., et al. (2018). Enzyme promiscuity drives branched-chain fatty acid synthesis in adipose tissues. Nat. Chem. Biol. *14*, 1021–1031.

Wyant, G.A., Abu-Remaileh, M., Wolfson, R.L., Chen, W.W., Freinkman, E., Danai, L. V., Vander Heiden, M.G., and Sabatini, D.M. (2017). mTORC1 Activator SLC38A9 Is Required to Efflux Essential Amino Acids from Lysosomes and Use Protein as a Nutrient. Cell *171*, 642-654.e12.

Xiong, J., He, J., Xie, W.P., Hinojosa, E., Ambati, C.S.R., Putluri, N., Kim, H.E., Zhu, M.X., and Du, G. (2019). Rapid affinity purification of intracellular organelles using a twin strep tag. J. Cell Sci. *132*.

Zhang, Z., Chen, W., Zhao, Y., and Yang, Y. (2018). Spatiotemporal Imaging of Cellular Energy Metabolism with Genetically-Encoded Fluorescent Sensors in Brain. Neurosci. Bull. *34*, 875–886.

Zhao, S., Torres, A., Henry, R.A., Trefely, S., Wallace, M., Lee, J. V, Carrer, A., Sengupta, A., Campbell, S.L., Kuo, Y.-M., et al. (2016). ATP-Citrate Lyase Controls a Glucose-to-Acetate Metabolic Switch. Cell Rep. *17*, 1037–1052.

Zhao, S., Jang, C., Liu, J., Uehara, K., Gilbert, M., Izzo, L., Zeng, X., Trefely, S., Fernandez, S., Carrer, A., et al. (2020). Dietary fructose feeds hepatic lipogenesis via microbiota-derived acetate. Nature.

bioRxiv preprint doi: https://doi.org/10.1101/2020.07.30.229468; this version posted July 30, 2020. The copyright holder for this preprint (which was not certified by peer review) is the author/funder, who has granted bioRxiv a license to display the preprint in perpetuity. It is made available under aCC-BY-NC 4.0 International license.

Figure Legends

Figure 1: SILEC-SF uses whole cell internal standards to reveal compartment specific acyl-CoA profiles

A) $^{15}N_1{}^{13}C_3$-isotope labeled vitamin B5 (VB5) is incorporated into coenzyme A (CoA) such that acyl-CoA species across all acyl (R group) species are isotope labeled. **B)** Representation of SILEC-SF workflow: internal standards were generated through isotope labeling, internal standard was added to samples as whole cells prior to cell lysis and separation of sub-cellular compartments by fractionation. The analyte and internal standard in each fraction was analyzed simultaneously by LC-MS and relative quantities are determined between samples. **C-F)** Acyl-CoA quantitation in whole cell lysate (WCL), mitochondria, cytosol and debris (remainder material). **C)** Brown adipocytes in cell culture (n=4 replicate dishes) **D)** *Acly*-/- mouse embryonic fibroblasts were incubated in DMEM supplemented with 10% dialyzed FBS and 1 mM acetate for 4 h before cell harvest (n=4 replicate dishes) **E)** Mouse liver tissue (n=6 mice) **E)** Transmural left ventricle of human heart (n=5 replicate samples from a single heart). Mean values from replicate samples are displayed and error bars show standard deviation. Some metabolites indicated in the legend for **C,E** and **F** were not quantified in the mitochondrial fraction. These were **C)** HMG-CoA, **E)** Malonyl-CoA and **F)** CoASH. (iso)Butyryl-CoA = Butyryl-CoA/Isobutyryl-CoA, (iso)Valeryl-CoA = Valeryl-CoA/Isovaleryl-CoA (isomers are not distinguished in analysis). HMG-CoA = 3-hydroxy-3-methylglutaryl-CoA. Data for all acyl-CoA species that were quantified in each fraction are displayed. Those that were not quantified showed insufficient signal intensity for the analyte, the internal standard or both.

Supplementary Figure 1

A) Schematic representation of standard curve generation. Sub-cellular fractions were generated from equal aliquots of SILEC internal standard cells processed in parallel to the experimental + SILEC cell samples. After fractionation, known quantities of unlabeled standards were added to build standard curves. **B**) Comparison of standard curves generated in different subcellular matrices across several acyl-CoA species in HepG2 cells using mitochondrial/cytosol protocol (upper panel) or nuclear / non-nuclear protocol (lower panel). WCL = whole cell lysate, Cyto = cytosol, mito = mitochondria, Non-nuc = non-nuclear fraction, nuc = nuclear fraction. **C)** Raw signal intensity for unlabeled acyl-CoAs are displayed across a range of concentrations in the presence of different sub-cellular matrices generated from fully labeled Hepa1c17 SILEC cells separated into different fractions. Unlableled acyl-CoAs were added after extraction of SILEC matrices, immediately before sample analysis, to test the impact of matrix effects on acquisition by LC-MS. **D)** Graphical representation of the 2 differential fractionation methods used in this study**.** Fully labeled SILEC cells were scraped into the appropriate fractionation buffer and mixed to make a homogenous cell suspension before addition in equal aliquots to cell (or tissue) samples. **E**) Acyl-CoA quantitation profiles from direct extraction of whole cells into trichloroacetic acid. Brown adipocytes were in regular culture media, same as in **figure 1C. F-I)** Western blot analysis of protein distribution. Equal protein quantity was loaded for each fraction. **F)** Hepa1c17 fractionation **G)** Brown adipocytes were fractionated using different numbers of strokes for optimization. 20 strokes was used for experiments. **H)** Liver tissue

bioRxiv preprint doi: https://doi.org/10.1101/2020.07.30.229468; this version posted July 30, 2020. The copyright holder for this preprint (which was not certified by peer review) is the author/funder, who has granted bioRxiv a license to display the preprint in perpetuity. It is made available under aCC-BY-NC 4.0 International license.

combined with SILEC HepG2 cells. **I)** Human heart fractionation for heart only, and heart combined with SILEC Hepa1c17 cell internal standard. CS (citrate synthase), VDAC (voltage dependent anion channel), FAS (fatty acid synthase), ACSS2 (Acyl-CoA synthetase short chain family member 2), ACLY (ATP-citrate lyase).

Figure 2: SILEC-SF detects distinct mitochondrial adaptation to hypoxia

A) Schematic comparing glutamine metabolism in the TCA cycle under hypoxic and normoxic conditions. Hypoxia promotes reductive carboxylation, which directs glutamine incorporation into citrate and away from succinyl-CoA. **B-D)** HepG2 cells were incubated under 20% (normoxia) or 1% (hypoxia) for 24 h. Cells were serum starved under the same oxygen tension in DMEM containing 5 mM glucose and 2 mM glutamine for 2 h before harvest. Appropriate enrichment of mitochondria and cytosol upon fractionation was assessed by examining enrichment of marker proteins in subcellular fractions by Western blot (**supp. 2E**). **B)** Succinyl-CoA quantitation in whole cell lysate (WCL), mitochondrial and cytosolic fractions. Symbols indicate individual replicate dishes (n=4) from a representative experiment. **C)** Fold-change (hypoxia/normoxia) from mean absolute quantitation as pmol/cell were calculated for 3 independent experiments conducted on separate days and log transformed. Symbols indicate the mean from each experiment. **D)** Representative experiment comparing profiles of short chain acyl-CoA species quantified in each fraction for n=4 replicate cell dishes. **B-D)** Error bars represent standard deviation. BH(I)B-CoA =3-Hydroxybutyryl-CoA/ 3-Hydroxyisobutyryl-CoA, (iso)Butyryl-CoA = Butyryl-CoA/Isobutyryl-CoA (isomers are not distinguished in analysis). For comparison between two groups, datasets were analyzed by two-tailed Student's *t*-test with Welch's correction and statistical significance was defined as $p < 0.05$ (*), $p < 0.01$ (**).

Supplementary Figure 2

HepG2 cells were incubated under 20% (normoxia) or 1% (hypoxia) for 24 h. Cells were serum starved under the same oxygen tension in DMEM containing 5 mM glucose and 2 mM glutamine for 2 h before harvest. **A-D)** Representative experiment showing quantitation in whole cell lysate (WCL), mitochondrial, cytosolic and debris fractions. Symbols represent individual replicate dishes (n=4) and error bars represent standard deviation. Lower abundance metabolites are magnified in the upper right corner of each panel. **E)** Western blots comparing protein enrichment for representative marker proteins for mitochondria, cytosol and nucleus. HepG2 cells were subject to sub-cellular fractionation by both the mitochondrial/cytosol and nuclear/non-nuclear protocols. Equal protein quantity was loaded for each fraction. VDAC (voltage dependent anion channel), SUCLA2 (Succinyl-CoA ligase [ADP-Forming] subunit beta), SUCLG1 (Succinyl-CoA ligase [GDP-forming] subunit alpha), OGDH (oxoglutarate dehydrogenase), FAS (fatty acid synthase), ACSS2 (Acyl-CoA synthetase short chain family member 2), ACLY (ATP-citrate lyase). For comparison between two groups, datasets were analyzed by two-tailed Student's *t*-test with Welch's correction and statistical significance defined as $p < 0.05$ (*), $p < 0.01$ (**), $p < 0.001$ (***), $p < 0.0001$ (****).

Figure 3: Cytosolic HMG-CoA is a sensitive readout of cytosolic acetate supply

A) Schematic representation of cytosolic acetyl-CoA generation. Acetate supplies cytosolic acetyl-CoA through upregulation of ACSS2 in ACLY deficient cells. Cytosolic acetyl-CoA

bioRxiv preprint doi: https://doi.org/10.1101/2020.07.30.229468; this version posted July 30, 2020. The copyright holder for this preprint (which was not certified by peer review) is the author/funder, who has granted bioRxiv a license to display the preprint in perpetuity. It is made available under aCC-BY-NC 4.0 International license.

has multiple fates including use as a substrate for HMG-CoA synthesis, which is a substrate for the mevalonate pathway. **B-D)** Cells were incubated for 4 h in DMEM supplemented with 10% dialyzed fetal calf serum with the addition of the indicated amount of acetate for 4 h. Whole cell acyl-CoA concentrations were determined in ACLY deficient mouse embryonic fibroblasts (*Acly*$^{-/-}$ MEFs) and liver cancer cell line (*Acly*$^{-/-}$ liver cancer cells) as well as matched ACLY sufficient control (*Acly*$^{f/f}$ liver cancer). Symbols represents individual replicate cell dishes (n=4) from representative experiments. Error bars show standard deviation. **B)** Whole cell direct extraction fold-change analysis. Fold change compared to mean 0 mM acetate concentration (in µM) was calculated and log transformed. **C)** Whole cell direct extraction (same as in **B**) displayed as cellular concentration for acetyl-CoA and HMG-CoA. **D)** SILEC-SF was used to specifically determine cytosolic acyl-CoA response to 0.1 versus 1 mM acetate supplementation. For comparison between two groups, datasets were analyzed by two-tailed Student's *t*-test with Welch's correction and statistical significance defined as $p < 0.05$ (*), $p < 0.01$ (**), $p < 0.001$ (***), $p < 0.0001$ (****).

Supplementary Figure 3

A) Western blot confirming ACLY deletion and ACSS2 upregulation in *Acly*$^{-/-}$ liver cancer cell line compared to control *Acly*$^{f/f}$ liver cancer cell line. Equal protein was loaded. **B-D)** Whole cell acyl-CoA concentrations were determined after direct extraction of cells incubated in DMEM supplemented with 10% dialyzed fetal calf serum with the addition of the indicated concentration of acetate for 4 h. Representative experiments are displayed. **B)** ACLY deficient mouse embryonic fibroblasts (*Acly*$^{-/-}$ MEFs). **C)** *Acly*$^{-/-}$ liver cancer cell line and **(D)** parental *Acly*$^{f/f}$ liver cancer control cells **(D)**. **E,F)** SILEC-SF was used to specifically determine cytosolic acyl-CoA response to 0.1 versus 1 mM acetate supplementation in *Acly*$^{-/-}$ MEFs **(E)** and *Acly*$^{-/-}$ liver cancer cells **(F)**. Data for all acyl-CoA species that were quantified in each fraction are displayed. Those that were not quantified showed insufficient signal intensity for the analyte, the internal standard or both. Low abundance metabolites are magnified in the upper right corner of each panel. **B-F)** Each symbol represents an individual replicate cell dish (n=4) from representative experiments. Error bars show standard deviation. For comparison between two groups, datasets were analyzed by two-tailed Student's *t*-test with Welch's correction and statistical significance defined as $p < 0.05$ (*), $p < 0.01$ (**), $p < 0.001$ (***), $p < 0.0001$ (****).

Figure 4: Propionyl-CoA is enriched in the nucleus and responds to serum starvation

A-B) HepG2 cells were incubated under 20% (normoxia) or 1% (hypoxia) for 24 h. Cells were serum starved under the same oxygen tension in DMEM containing 5 mM glucose and 2 mM glutamine for 2 h before harvest. **A)** Representative experiment comparing profiles of short chain acyl-CoA species quantified after nuclear/non-nuclear fractionation. Symbols represents individual replicate cell dishes (n=4). Error bars show standard deviation. Some metabolites indicated in the legend were not quantified in all fractions, specifically, crotonoyl-CoA was not quantified in WCL, nuclear and wash fractions and glutaryl-CoA, (iso)butyryl-CoA, and HMG-CoA were not quantified in the nuclear fraction. Those that were not quantified showed insufficient signal intensity for the analyte, the internal standard or both. **B)** Fold-change (propionyl-CoA/acetyl-CoA) in absolute quantitation as pmol/cell were calculated for 3 independent experiments conducted on separate days (n=4 individual replicate cell dishes within each

bioRxiv preprint doi: https://doi.org/10.1101/2020.07.30.229468; this version posted July 30, 2020. The copyright holder for this preprint (which was not certified by peer review) is the author/funder, who has granted bioRxiv a license to display the preprint in perpetuity. It is made available under aCC-BY-NC 4.0 International license.

experiment). Data was log transformed and statistics were calculated by Welch's t-test. Symbols indicate mean from each experiment, error bars show standard deviation. **C)** Schematic representation of propionyl-CoA generation. Propionyl-CoA is generated in the mitochondria from multiple sources including isoleucine. 3 of the 6 carbons in Ile contribute to the acyl group of propionyl-CoA. **D)** Nuclear acyl-CoA quantitation from HepG2 cells incubated in DMEM containing 5 mM glucose and 2 mM glutamine in the presence or absence of 10% serum for 23 h before SILEC-SF analysis. **E)** Pancreatic ductal adenocarcinoma cells were incubated in media containing uniformly labeled $^{13}C_6$-isoleucine 50% diluted with unlabeled isoleucine. Percent incorporation into propionyl-CoA M3 was determined for the indicated incubation times. Fractionation was performed with post-labeling in the presence of partially labeled $^{13}C_6$-isoleucine to account for post-harvest metabolism. For comparison between two groups, datasets were analyzed by two-tailed Student's *t*-test with Welch's correction and statistical significance defined as $p < 0.05$ (*), $p < 0.01$ (**).

Supplementary Figure 4

A-D) HepG2 cells were incubated under 20% (normoxia) or 1% (hypoxia) for 24 h. Cells were serum starved under the same oxygen tension in DMEM containing 5 mM glucose and 2 mM glutamine for 2 h before harvest. **E-G)** HepG2 cells were incubated in DMEM containing 5 mM glucose and 2 mM glutamine in the presence or absence of 10% serum for 23 h before SILEC-SF for acyl-CoA quantitation. **A-G)** Representative experiment comparing profiles of short chain acyl-CoA species quantified in each fraction. Symbols represents individual replicate cell dishes (n=4) from representative experiments. Error bars show standard deviation. Data for all short chain acyl-CoA species quantified in each fraction are displayed. Those that were not quantified showed insufficient signal intensity for the analyte, the internal standard or both. ND= not detected. Low abundance metabolites are magnified in the upper right corner of each panel**. H-J)** Incorporation of various substrates into propionyl-CoA, succinyl-CoA and acetyl-CoA was compared in whole cells by direct extraction of pancreatic adenocarcinoma cells incubated in media containing uniformly (U) ^{13}C-labeled substrates for 18 h. Total substrate concentrations were equal across all samples except for propionate, which was added only to the U$^{13}C_3$-propionate samples. U^{13}C-labeled Val, Leu and Ile were diluted 1:1 with unlabeled substrate. N=3 replicate samples per condition from a single experiment. Error bars are SD. For comparison between two groups, datasets were analyzed by two-tailed Student's *t*-test with Welch's correction and statistical significance defined as $p < 0.05$ (*), $p < 0.01$ (**).

bioRxiv preprint doi: https://doi.org/10.1101/2020.07.30.229468; this version posted July 30, 2020. The copyright holder for this preprint (which was not certified by peer review) is the author/funder, who has granted bioRxiv a license to display the preprint in perpetuity. It is made available under aCC-BY-NC 4.0 International license.

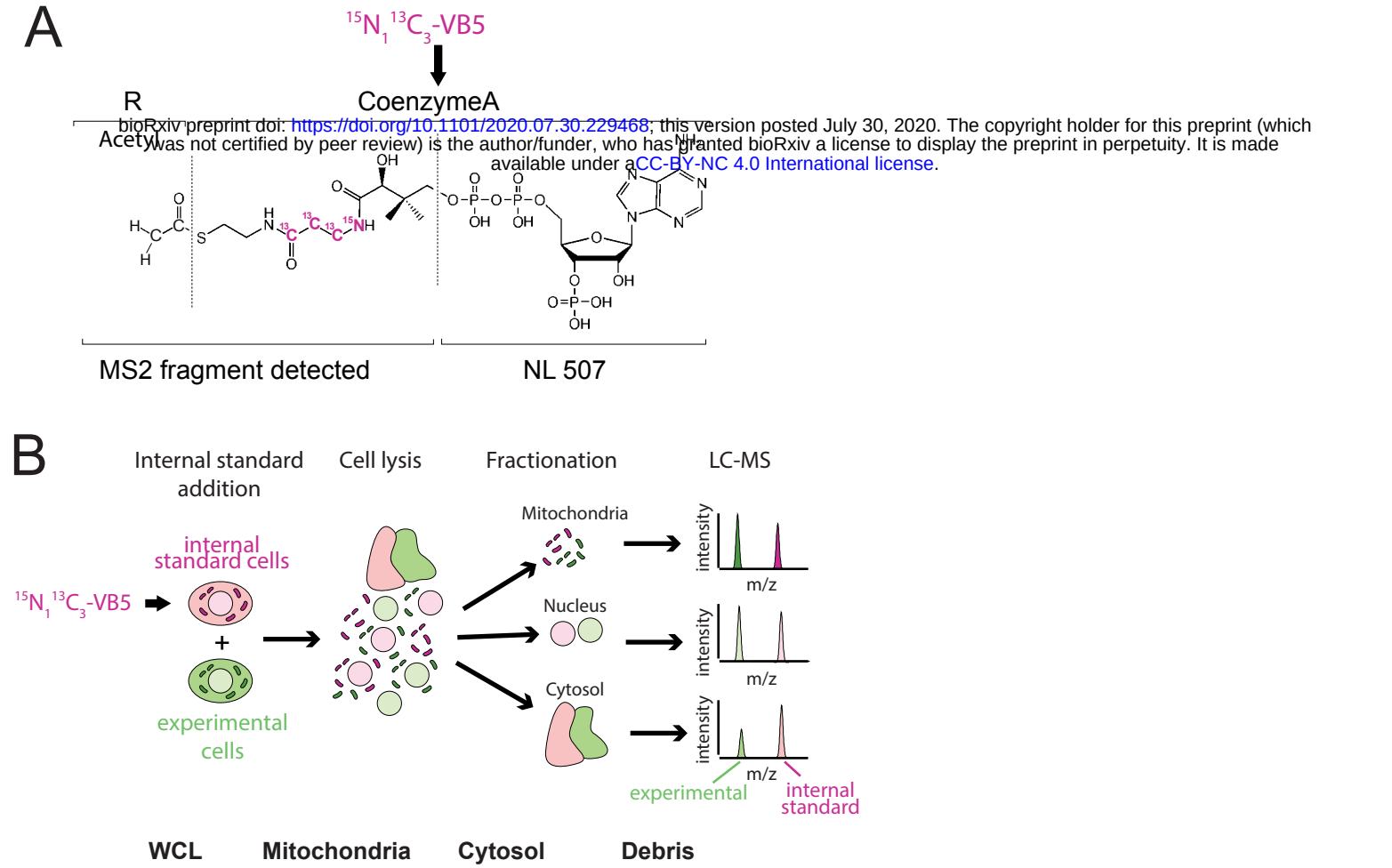

Figure 1: SILEC-SF uses whole cell internal standards to reveal compartment specific acyl-CoA profiles

bioRxiv preprint doi: https://doi.org/10.1101/2020.07.30.229468; this version posted July 30, 2020. The copyright holder for this preprint (which was not certified by peer review) is the author/funder, who has granted bioRxiv a license to display the preprint in perpetuity. It is made available under aCC-BY-NC 4.0 International license.

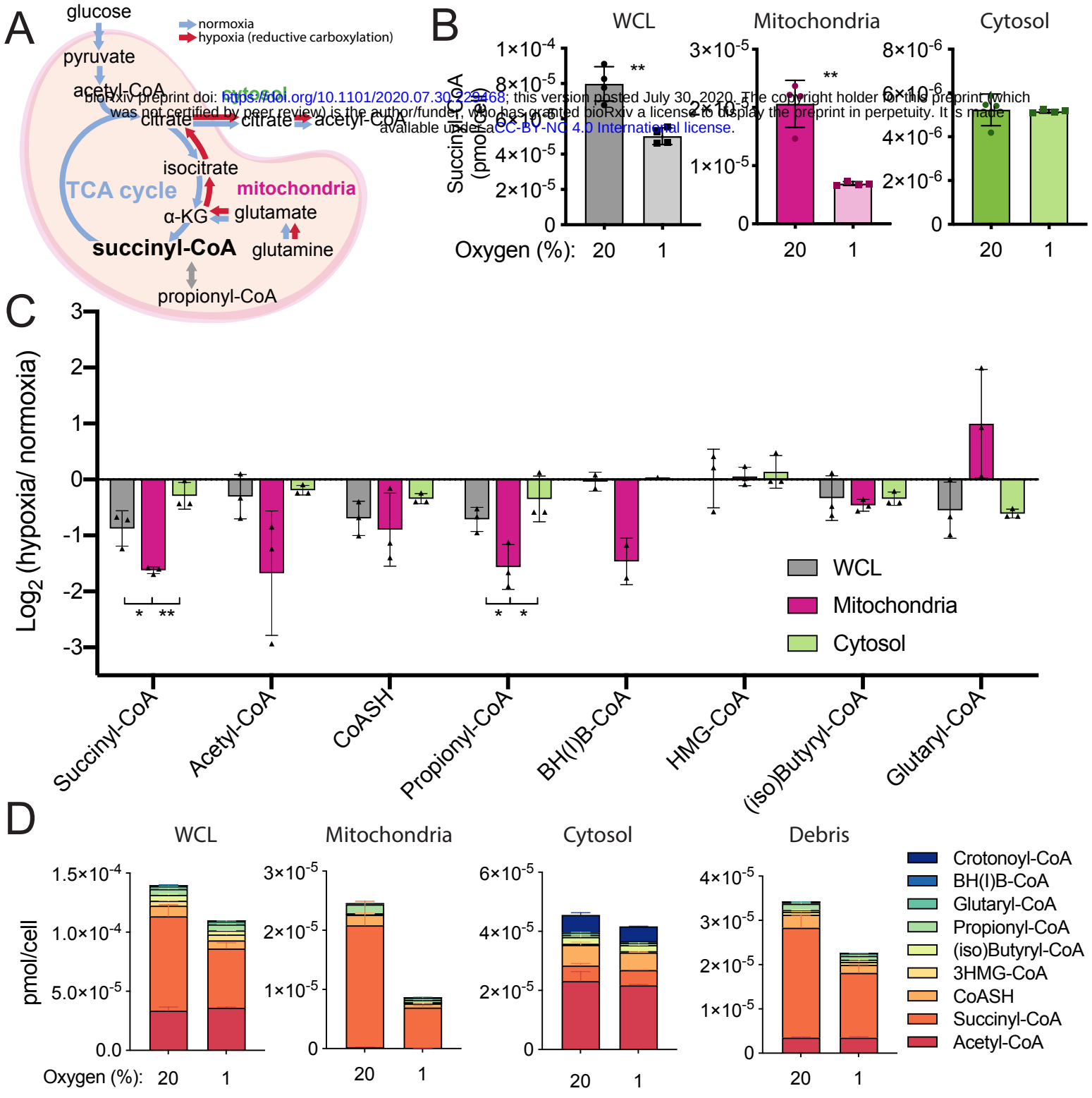

Figure 2: SILEC-SF detects distinct mitochondrial adaptation to hypoxia

bioRxiv preprint doi: https://doi.org/10.1101/2020.07.30.229468; this version posted July 30, 2020. The copyright holder for this preprint (which was not certified by peer review) is the author/funder, who has granted bioRxiv a license to display the preprint in perpetuity. It is made available under aCC-BY-NC 4.0 International license.

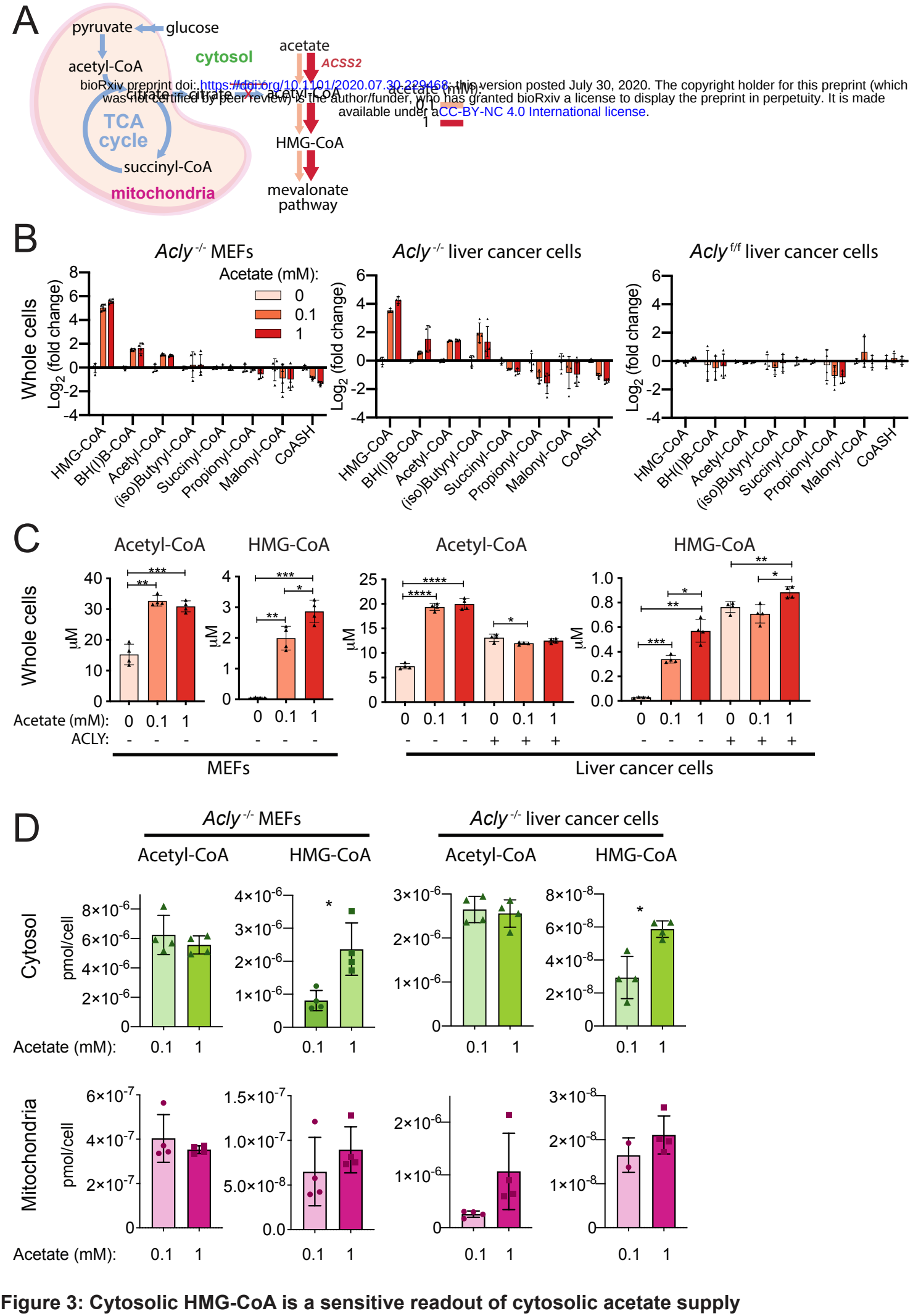

Figure 3: Cytosolic HMG-CoA is a sensitive readout of cytosolic acetate supply

bioRxiv preprint doi: https://doi.org/10.1101/2020.07.30.229468; this version posted July 30, 2020. The copyright holder for this preprint (which was not certified by peer review) is the author/funder, who has granted bioRxiv a license to display the preprint in perpetuity. It is made available under aCC-BY-NC 4.0 International license.

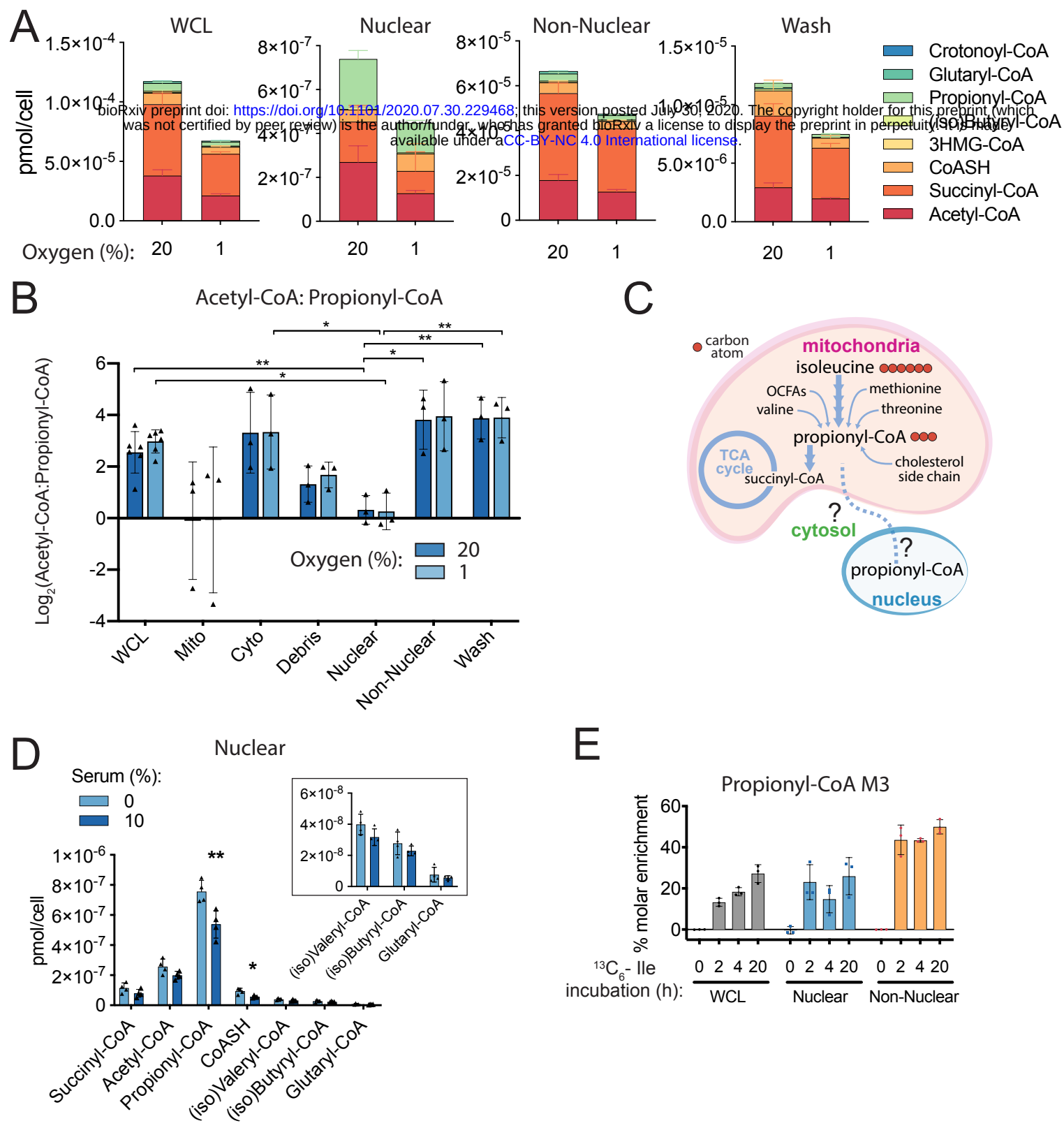

Figure 4: Propionyl-CoA is enriched in the nucleus and responds to serum starvation

Supplemental Figure 1

bioRxiv preprint doi: https://doi.org/10.1101/2020.07.30.229468; this version posted July 30, 2020. The copyright holder for this preprint (which was not certified by peer review) is the author/funder, who has granted bioRxiv a license to display the preprint in perpetuity. It is made available under aCC-BY-NC 4.0 International license.

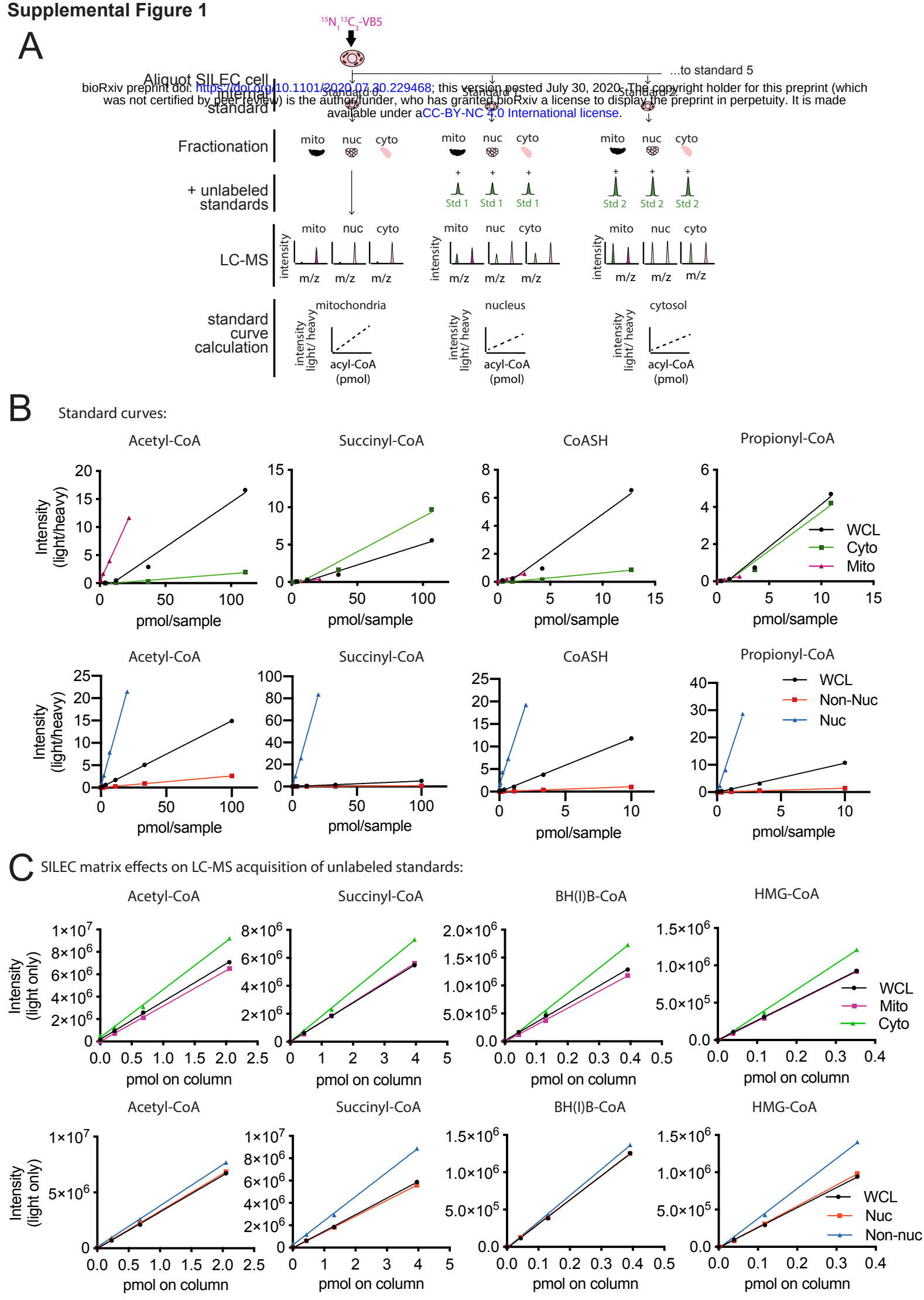

bioRxiv preprint doi: https://doi.org/10.1101/2020.07.30.229468; this version posted July 30, 2020. The copyright holder for this preprint (which was not certified by peer review) is the author/funder, who has granted bioRxiv a license to display the preprint in perpetuity. It is made available under aCC-BY-NC 4.0 International license.

Supplemental Figure 1

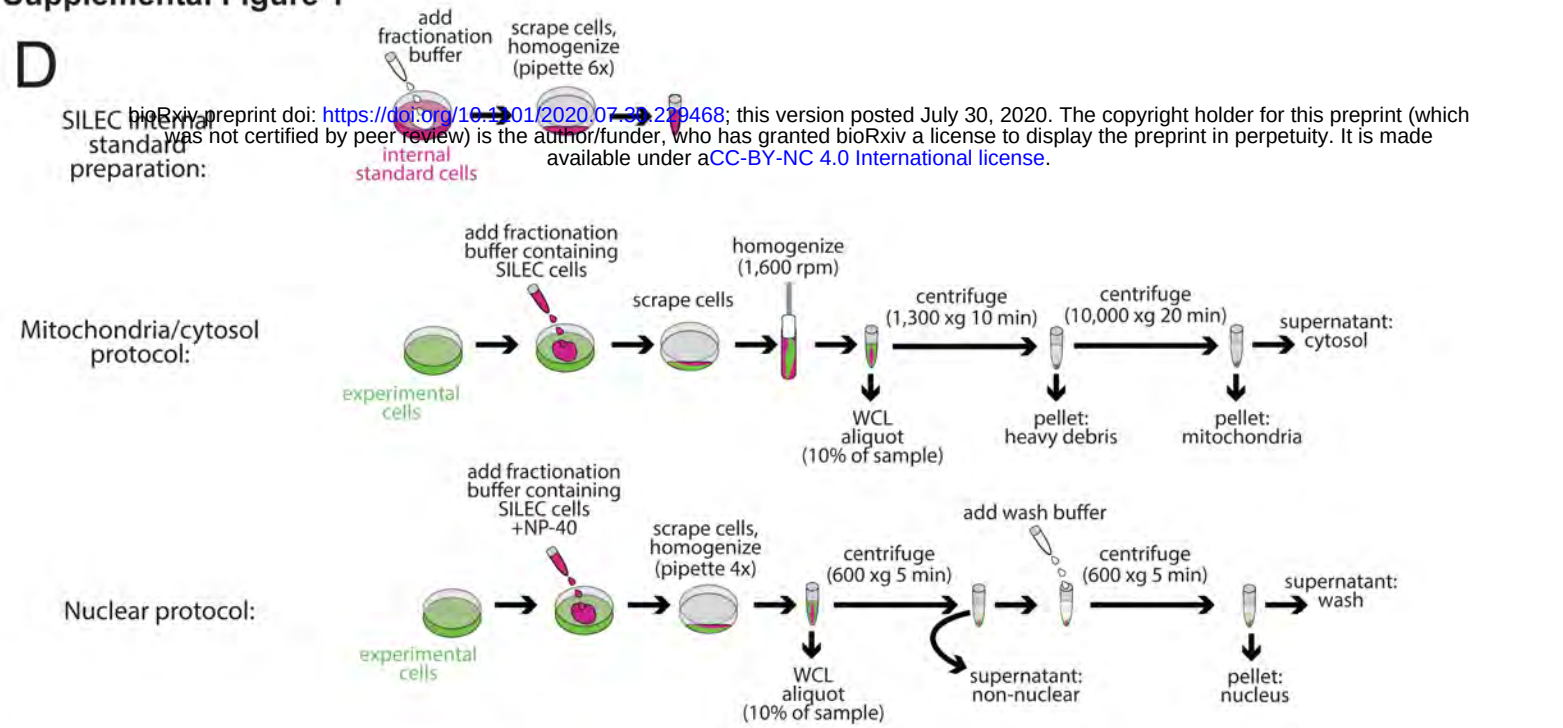

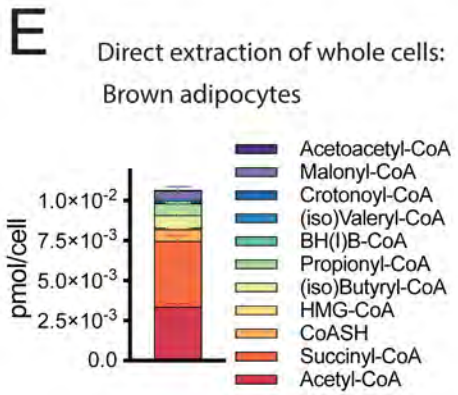

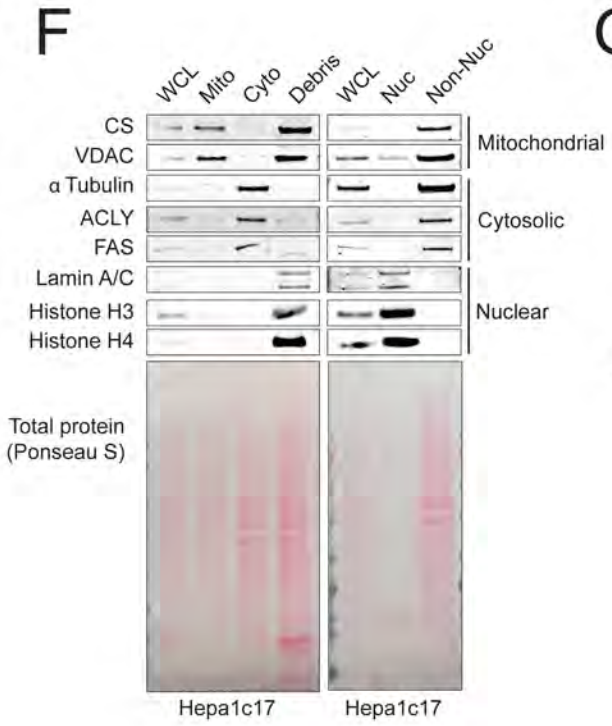

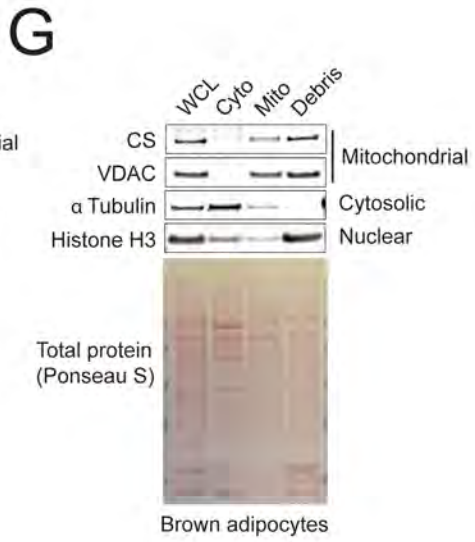

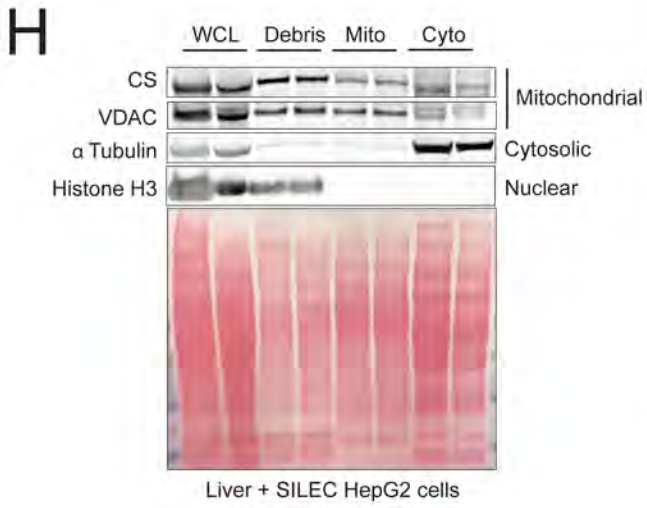

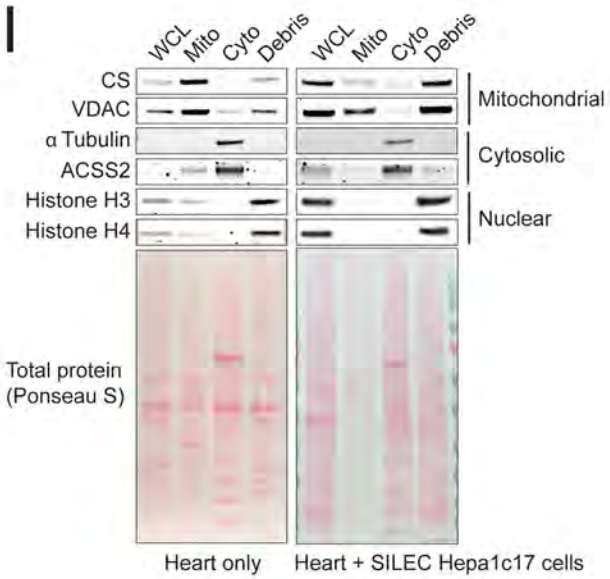

Supplemental Figure 2

bioRxiv preprint doi: https://doi.org/10.1101/2020.07.30.229468; this version posted July 30, 2020. The copyright holder for this preprint (which was not certified by peer review) is the author/funder, who has granted bioRxiv a license to display the preprint in perpetuity. It is made available under aCC-BY-NC 4.0 International license.

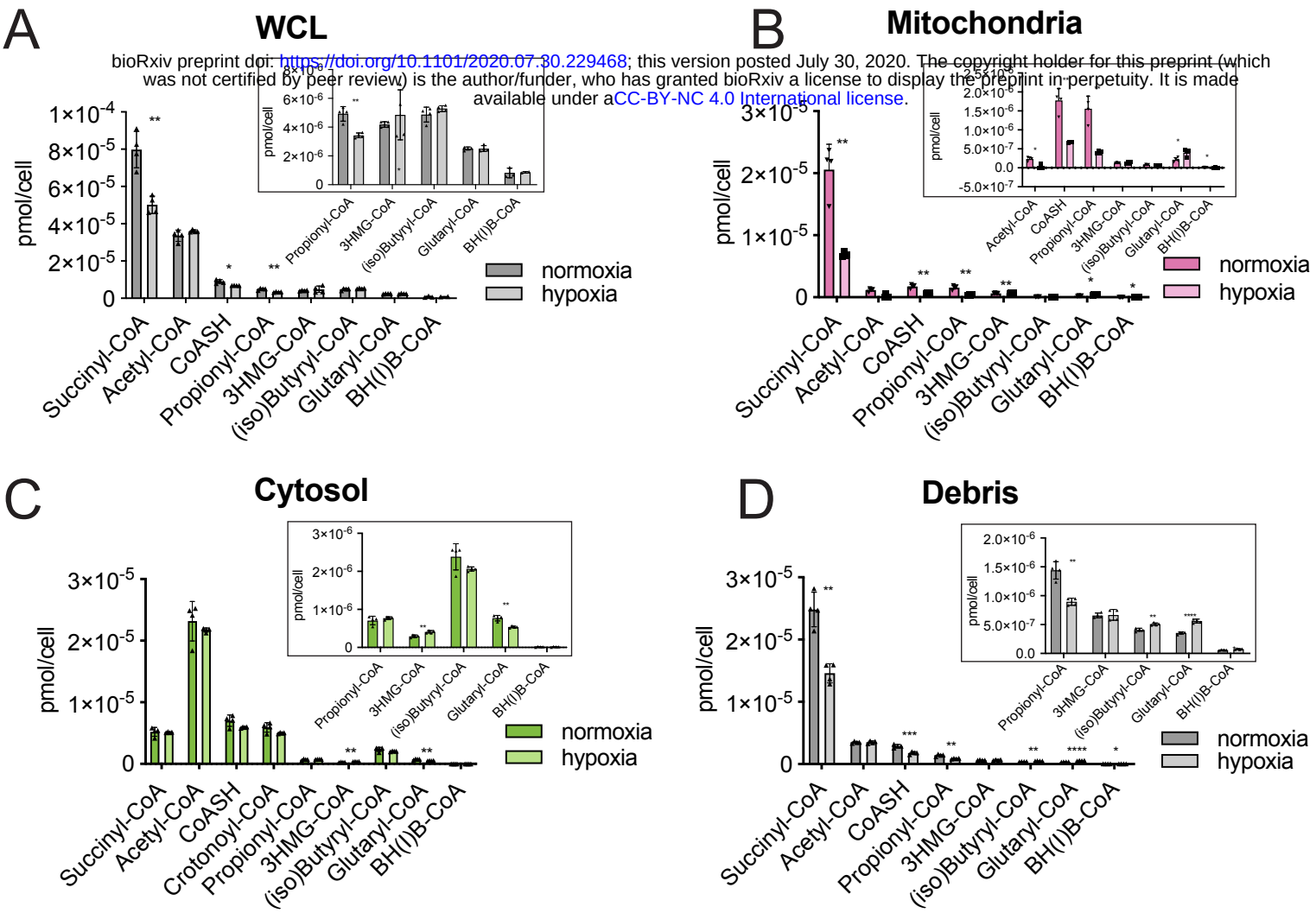

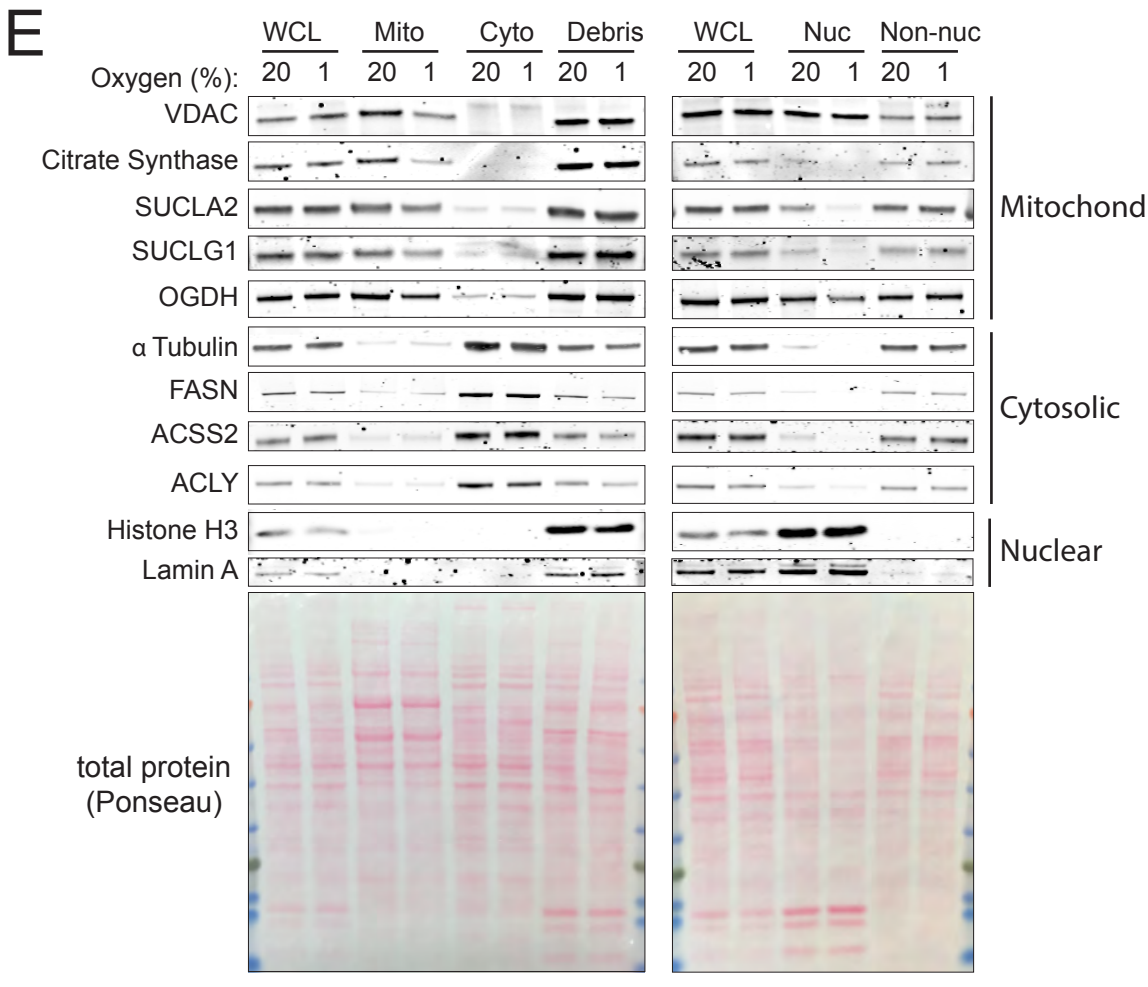

Supplemental Figure 3

bioRxiv preprint doi: https://doi.org/10.1101/2020.07.30.229468; this version posted July 30, 2020. The copyright holder for this preprint (which was not certified by peer review) is the author/funder, who has granted bioRxiv a license to display the preprint in perpetuity. It is made available under aCC-BY-NC 4.0 International license.

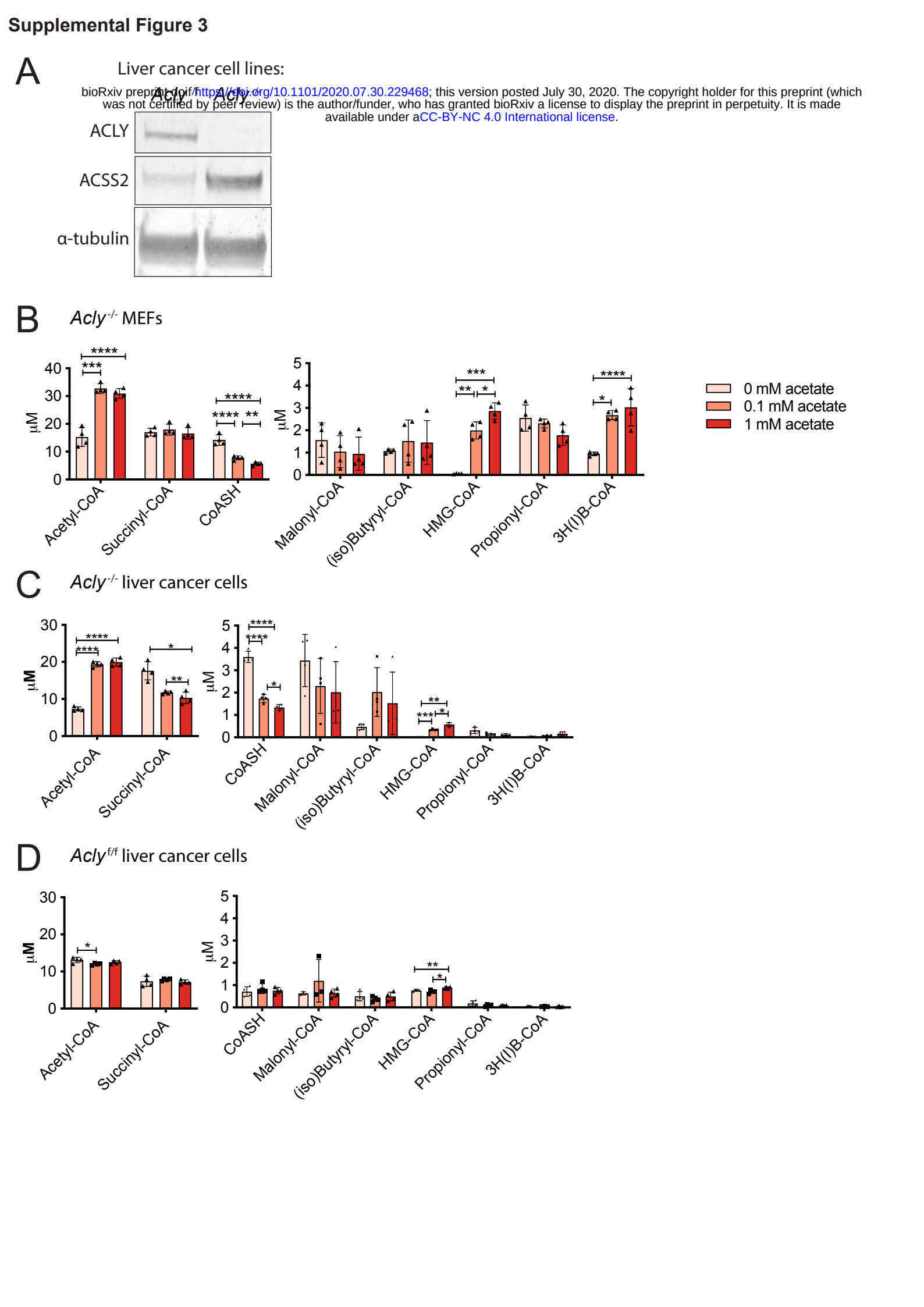

Supplemental Figure 3

bioRxiv preprint doi: https://doi.org/10.1101/2020.07.30.229468; this version posted July 30, 2020. The copyright holder for this preprint (which was not certified by peer review) is the author/funder, who has granted bioRxiv a license to display the preprint in perpetuity. It is made available under aCC-BY-NC 4.0 International license.

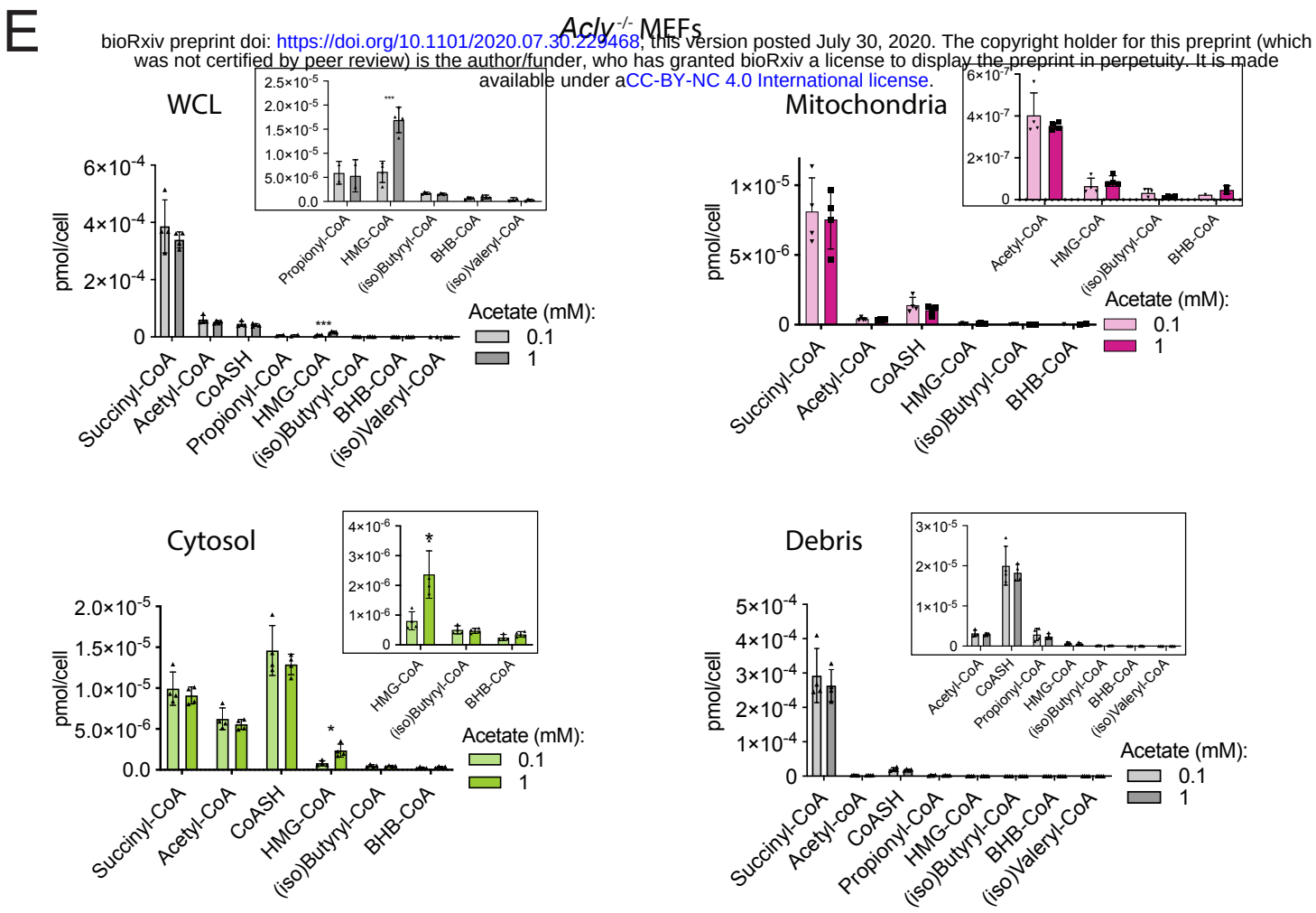

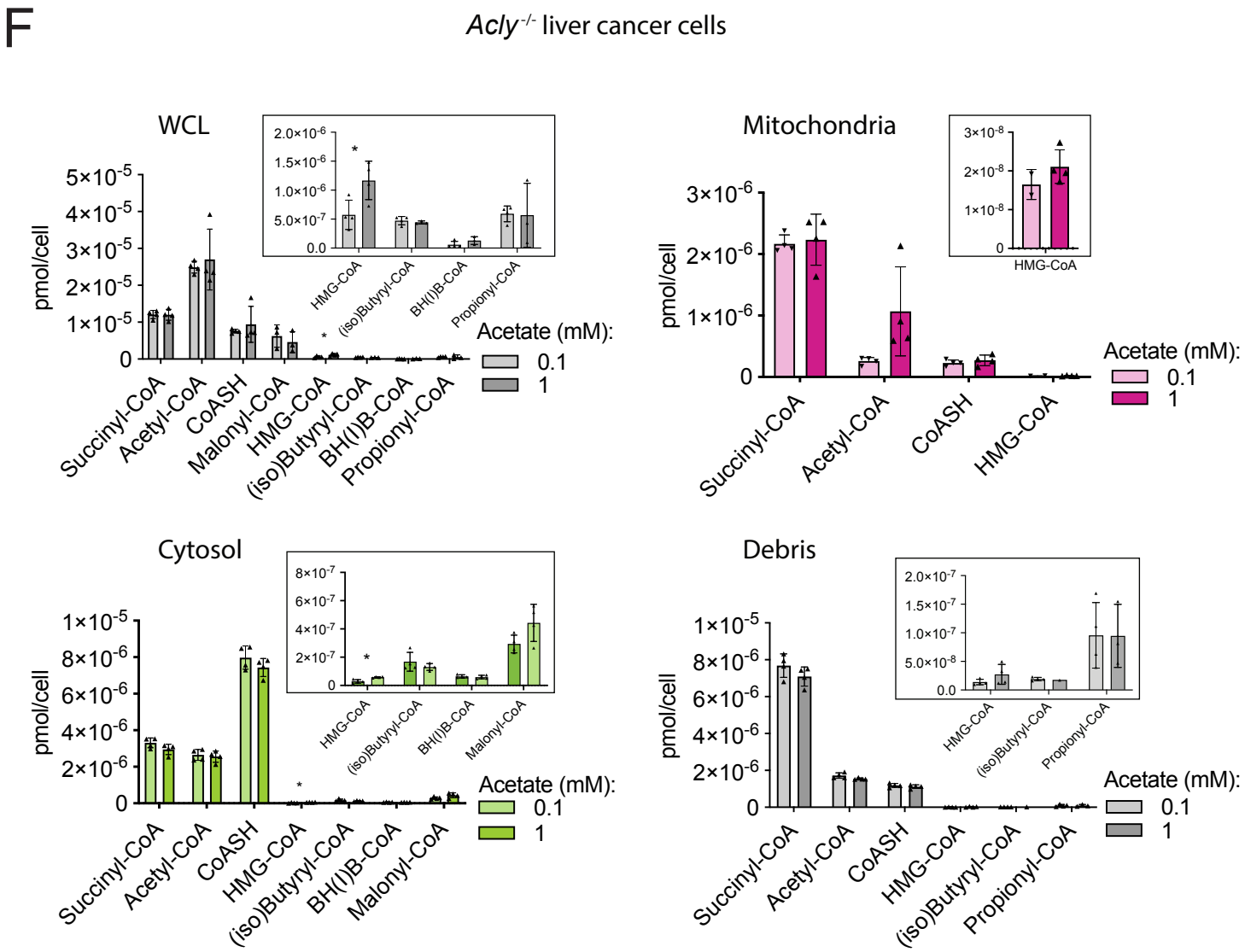

Supplemental Figure 4

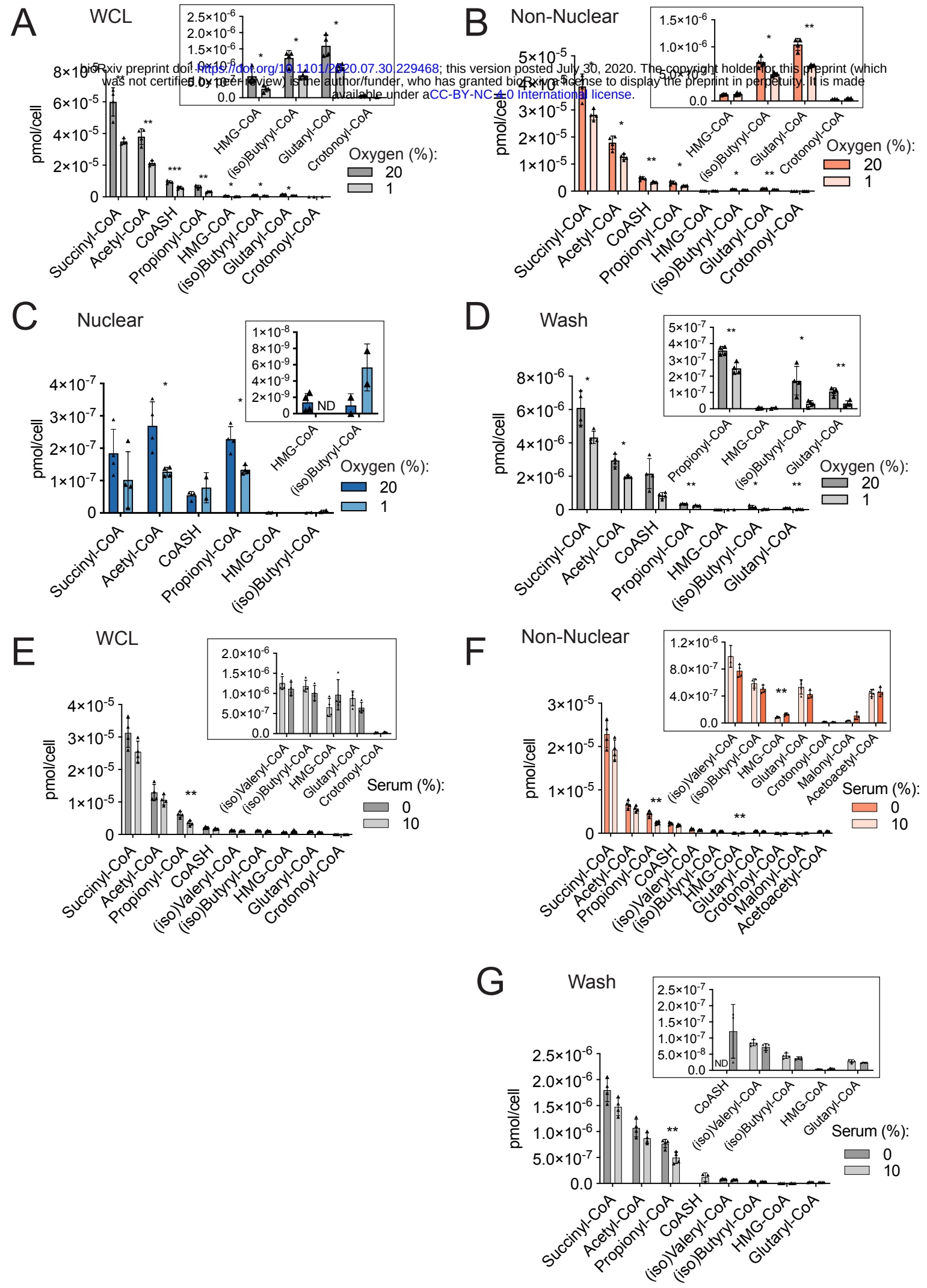

bioRxiv preprint doi: https://doi.org/10.1101/2020.07.30.229468; this version posted July 30, 2020. The copyright holder for this preprint (which was not certified by peer review) is the author/funder, who has granted bioRxiv a license to display the preprint in perpetuity. It is made available under aCC-BY-NC-4.0 International license.

Supplemental Figure 4

bioRxiv preprint doi: https://doi.org/10.1101/2020.07.30.229468; this version posted July 30, 2020. The copyright holder for this preprint (which was not certified by peer review) is the author/funder, who has granted bioRxiv a license to display the preprint in perpetuity. It is made available under aCC-BY-NC 4.0 International license.

H

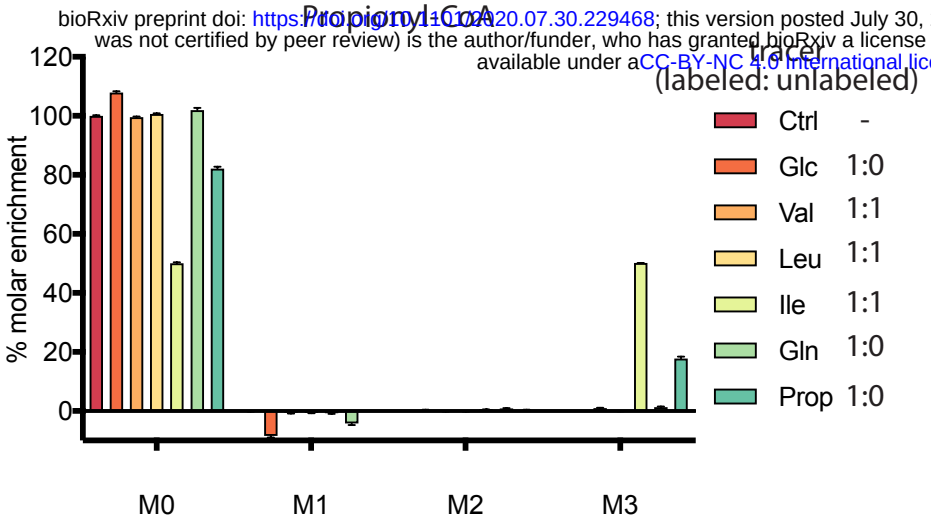

I

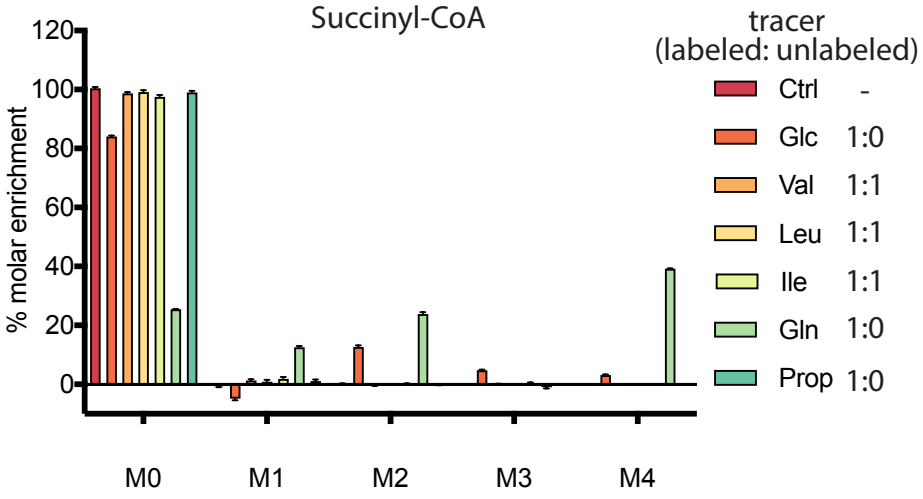

J